

A Frequency-domain Approach for the P_1 Approximation of Time-dependent Radiative Transfer

Mohamed Addam*, Abderrahman Bouhamidi†, Mohammed Seaid‡

Abstract

We propose a new frequency-domain method to solve the simplified P_1 approximation of time-dependent radiative transfer equations. The method employs the Fourier transform and consists of two stages. In the first stage the equations are transformed into an elliptic problem for the frequency variables. The numerical solutions of this problem are approximated using a Galerkin projection method based on the tensor-product B-spline interpolants. In the second stage a Gauss-Hermite quadrature procedure is proposed for the computation of the inverse Fourier transform to recover the numerical solutions of the original simplified P_1 problem. The method avoids the discretization of the time variable in the considered system and it accurately resolves all time scales in radiative transfer regimes. Several test examples are used to verify high accuracy, effectiveness and good resolution properties for smooth and discontinuous solutions.

Keywords. Radiative transfer; Simplified P_1 approximation; Frequency-domain method; Galerkin projection; Gauss-Hermite quadrature; tensor-product B-spline interpolation

1 Introduction

Transient radiative transfer problems have important presence in a variety of physical and engineering areas such as nuclear reactors, gas-turbine combustion chambers, glass manufacturing and radiation hydrodynamics [21]. General details on physical and mathematical descriptions of these models have been addressed in a number of books and papers [22, 21, 19, 30] among others. Despite the equation governing the transient radiative transfer is linear, computing its numerical solution is not trivial due to:

- (i) The large number of dependent unknowns. In general, the solution in the transient radiative transfer is a function of eight independent variables, three space variables, three angle variables, one energy variable, and one time variable. After discretizing these variables the computer memory requirements and the computational cost become drastically immense. This imposes severe restrictions on computational methods for transient radiative transfer.
- (ii) In many applications in transient radiative transfer, the solution is not a smooth function of the dependent variables. Steep fronts and even shocks can arise, which need to be resolved accurately in applications and often cause severe numerical difficulties.
- (iii) It is well known that the radiative transfer equation changes the behavior from a physical situation to another. For example, the radiative transfer equation behaves like hyperbolic in void-like regions; in optically dense region, it behaves like elliptic for steady-state case and parabolic for time-dependent case. To construct an unified computational algorithm that resolve accurately all the behavior cases is extremely difficult.

*Université Lille-Nord de France, ULCO, L.M.P.A, F-62228 Calais-Cedex, France (addam@lmpa.univ-littoral.fr)

†Université Lille-Nord de France, ULCO, L.M.P.A, F-62228 Calais-Cedex, France (bouhamidi@lmpa.univ-littoral.fr)

‡School of Engineering and Computing Sciences, University of Durham, South Road, Durham DH1 3LE, UK (m.seaid@durham.ac.uk)

The most accurate procedures available in the literature for computing radiative transfer are the zonal and Monte Carlo methods [22]. However, these methods are not widely applied in comprehensive radiative transfer calculations due to their large computational time and storage requirements. The S_n discrete-ordinate methods [8] appear to be reasonable compromises for solving the radiative transfer equations, but still one has to deal with large systems of algebraic equations, resulting from discretizing angle and space coordinates, that may be detrimental to the efficiency of the numerical solver if the radiative transfer equations are to be solved in conjunction with those of material, momentum, energy transport and chemical reactions as a fully coupled system, compare [25, 28] and further references are therein.

Approximate models for radiative transfer have also been derived and widely used in the literature. As examples for such approximations we cite the simplified P_N equations, see [17] among others. These simplified models are derived for steady-state radiative transfer using asymptotic analysis and they perform very well when the medium under consideration is isotropic and optically thick (opaque). In fact, in an opaque medium the system is close to a radiative equilibrium for which assumptions of diffusion and simplified P_N equations are satisfied. The simplified P_N approximations were first proposed in [11] and theoretically studied in [16]. In [17, 29] the simplified P_N approximations have been extensively studied for radiative transfer in glass manufacturing, while in [28] they have been implemented for radiation in hydrodynamics. The simplified P_N approximations have also been studied in [13] for radiative transfer in tissue, in [14] for fluorescence tomography, in [5] for internal radiation in crystal growth, and in [15] for photon and electron radiotherapy. Extension of simplified P_N approximations to time-dependent radiative transfer problems has been carried out in [9] using a formal asymptotic analysis. In the current study, we consider the time-dependent simplified P_1 approximation to the transient radiative transfer problems in two space dimensions. The main advantage in considering the simplified P_N approximations is the fact that the transient radiative transfer equation is transformed to a mixed set of parabolic equations independent of the angular directions, facilitating their numerical solution. Furthermore, comparisons presented in the previous references for steady-state simulations, proved that in optically thick media (large absorption) the simplified P_N models approximate the full radiative transfer problem with a very low computational cost.

Traditionally, solving the simplified P_1 approximation using explicit time-domain methods requires extremely small time stepsizes because of the large velocity in the radiative signals. In [9], solution of the time-dependent simplified P_1 approximation is obtained in the space-time formulation by using a linearly implicit time-marching scheme of Rosenbrock type. Although these methods are effective in solving wide range of practical problems, one of major drawbacks of these algorithms would come from the fact that they are not naturally parallelizable. This paper presents (i) a simplified formulation for dynamic analysis of radiative signals in the frequency domain and (ii) a technique for obtaining transient responses from frequency-dependent solutions. Although the considered frequency-domain formulation requires the use of Fourier transform and Laplace transform if time solutions are needed, its implementation is generally simpler than for the time-domain formulation. Our goal in the present work is to develop robust and efficient solvers for the transient radiative transfer problems. This is achieved by coupling the simplified P_1 approximation in the modeling part and the frequency-domain method for the solution part. Solving coupled radiative transport-diffusion problems in optical tomography using a class of frequency-domain methods has been investigated in [12, 27] among others. In these references, authors used the standard Galerkin finite element methods to discretize the considered radiative transport-diffusion problems in the frequency domain. In the current study we consider a different approach based on the Galerkin B-spline techniques. To the best of our knowledge, solving the time-dependent simplified P_1 problems using these techniques is reported for the first time. The proposed frequency-domain method is also applied to the transient simplified P_1 approximation of radiative heat transfer problems. The performance of this algorithm is illustrated by numerical examples for time-dependent radiative transfer in presence of both smooth and shock solutions. The results obtained demonstrate good shock resolution with high accuracy in smooth regions and without any nonphysical oscillations near the shock areas. From a practical point of view, the performance of our frequency-domain method is very attractive because the computed solutions remain stable and highly accurate even on coarse grids without solving nonlinear problems.

The present paper is organized as follows. In section 2 we present the governing equations for the simplified P_1 approximation of time-dependent radiative transfer problems. The frequency-domain approach is formulated in section 3. This section includes both the Galerkin projection method using the tensor-product B-spline interpolants and the Gauss-Hermite quadrature procedure for the inverse Fourier transform. We also discuss the algorithmic aspect of the proposed method. Section 5 contains numerical results and applications. Conclusions are summarized in section 6.

2 Simplified P_1 Approximation of Radiative Transfer

Let $[0, T]$ be a time interval and Ω be a geometrical domain in \mathbb{R}^d , ($d \geq 2$) with boundary $\partial\Omega$ of an absorbing, scattering and emitting material. The dimensionless mono-energetic radiative transfer problem we consider in the current work reads

$$\frac{\varepsilon^2}{\mathcal{V}} \frac{\partial \psi}{\partial t} + \varepsilon \hat{\mathbf{s}} \cdot \nabla \psi + \sigma \psi = \frac{\sigma - \varepsilon^2 \sigma_a}{4\pi} \int_{\mathbb{S}^2} \psi d\hat{\mathbf{s}} + \frac{\varepsilon^2}{4\pi} q(t, \mathbf{x}), \quad (t, \mathbf{x}, \hat{\mathbf{s}}) \in (0, T] \times \Omega \times \mathbb{S}^2, \quad (2.1)$$

subject to the boundary condition

$$\psi(t, \xi, \hat{\mathbf{s}}) = \psi_b(t, \xi, \hat{\mathbf{s}}), \quad (t, \xi, \hat{\mathbf{s}}) \in (0, T] \times \Gamma^- \times \mathbb{S}^2, \quad (2.2)$$

and the initial condition

$$\psi(0, \mathbf{x}, \hat{\mathbf{s}}) = \psi_0(\mathbf{x}, \hat{\mathbf{s}}), \quad (\mathbf{x}, \hat{\mathbf{s}}) \in \Omega \times \mathbb{S}^2, \quad (2.3)$$

where $\psi = \psi(t, \mathbf{x}, \hat{\mathbf{s}})$ is the spectral intensity which is a function of time t , space \mathbf{x} and direction $\hat{\mathbf{s}}$, and it is traveling with the speed \mathcal{V} . Here, \mathbb{S}^2 is the unit sphere, σ_a is the absorption coefficient, σ is the sum of the absorption cross section σ_a and the scattering cross section σ_s ($\sigma = \sigma_a + \sigma_s$), ε is a scale parameter related to the optical thickness of the medium and assumed to be small, ψ_b is a given boundary intensity, ψ_0 is a given initial data and $q(t, \mathbf{x})$ is a source term which may depend on the medium temperature as well. Note that in the equation (2.1), the scattering phase function is assumed to be isotropic. For further physical and mathematical details on radiative transfer and related issues we refer the reader to [19, 22, 21, 23] among others. In (2.2), the boundary region Γ^- is defined by

$$\Gamma^- = \left\{ \xi \in \partial\Omega : \quad \mathbf{n}(\xi) \cdot \hat{\mathbf{s}} \leq 0 \right\},$$

where $\mathbf{n}(\xi)$ denotes the outward normal in ξ with respect to $\partial\Omega$. Note that, the above boundary and initial conditions for the radiative transfer equation are considered only for simplicity in presentation. However, other boundary and initial conditions for the radiative transfer equation (2.1) can also be incorporated in our formulation without major conceptual modifications.

The equations (2.1)-(2.3) are widely accepted as an accurate model for radiation transport in participating and non-participating media. These equations do not have analytical solutions for arbitrary geometries and their numerical solutions lead to computationally demanding problems due to the large set of dependent variables. Numerous investigations are currently being carried out to derive approximate, computationally less demanding than solving the equations (2.1)-(2.3). Among typical approximations to radiation transport we cite, diffusion approach [18], simplified P_N approximations [9, 10] and the entropy model [4]. Indeed, a major reduction of the discrete phase-space can be achieved, if one replaces the radiative transfer equation by a new model which only involves physical quantities independent of the angular direction. One possibility to do so is the usage of the so-called simplified P_N approximations. For the sake of completeness we shortly recapitulate how these approximations can be derived from an asymptotic analysis of the radiative transfer equation [17, 9].

The starting point is to rewrite the equation (2.1) as

$$(1 + \varepsilon \hat{\mathbf{s}} \cdot \mathcal{D}_{\mathbf{x}} + \varepsilon^2 \mathcal{D}_t) \psi = Q,$$

where

$$\mathcal{D}_{\mathbf{x}} = \frac{1}{\sigma} \nabla, \quad \mathcal{D}_t = \frac{1}{\sigma \mathcal{V}} \frac{\partial}{\partial t}, \quad Q = \frac{1}{4\pi\sigma} \left((\sigma - \varepsilon^2 \sigma_a) \phi + \varepsilon^2 q \right), \quad (2.4)$$

and $\phi(t, \mathbf{x})$ is the mean radiative intensity defined by

$$\phi(t, \mathbf{x}) = \int_{\mathbb{S}^2} \psi(t, \mathbf{x}, \hat{\mathbf{s}}) d\hat{\mathbf{s}}. \quad (2.5)$$

Then, we apply a Neumann series to formally invert the transport operator

$$\begin{aligned} \psi &= (1 + \varepsilon \hat{\mathbf{s}} \cdot \mathcal{D}_{\mathbf{x}} + \varepsilon^2 \mathcal{D}_t)^{-1} Q, \\ &\approx \left(1 - (\hat{\mathbf{s}} \cdot \mathcal{D}_{\mathbf{x}}) \varepsilon + \left((\hat{\mathbf{s}} \cdot \mathcal{D}_{\mathbf{x}})^2 - \mathcal{D}_t \right) \varepsilon^2 + \left((\hat{\mathbf{s}} \cdot \mathcal{D}_{\mathbf{x}}) \mathcal{D}_t + \left(\mathcal{D}_t - (\hat{\mathbf{s}} \cdot \mathcal{D}_{\mathbf{x}})^2 \right) (\hat{\mathbf{s}} \cdot \mathcal{D}_{\mathbf{x}}) \right) \varepsilon^3 \right. \\ &\quad \left. + \left((\mathcal{D}_t - (\hat{\mathbf{s}} \cdot \mathcal{D}_{\mathbf{x}})^2) \mathcal{D}_t + \left(-2 (\hat{\mathbf{s}} \cdot \mathcal{D}_{\mathbf{x}}) \mathcal{D}_t + (\hat{\mathbf{s}} \cdot \mathcal{D}_{\mathbf{x}})^3 \right) (\hat{\mathbf{s}} \cdot \mathcal{D}_{\mathbf{x}}) \right) \varepsilon^4 + \dots \right) Q. \end{aligned} \quad (2.6)$$

Integrating with respect to $\hat{\mathbf{s}}$ over all directions in the unit sphere \mathbb{S}^2 and using the relation

$$\begin{aligned} \int_{\mathbb{S}^2} (\hat{\mathbf{s}} \cdot \mathcal{D}_{\mathbf{x}})^n d\hat{\mathbf{s}} &= \left(1 + (-1)^n \right) \frac{2\pi}{n+1} \mathcal{D}_{\mathbf{x}}^n, \\ &= \left(1 + (-1)^n \right) \frac{2\pi}{n+1} (\mathcal{D}_{\mathbf{x}} \cdot \mathcal{D}_{\mathbf{x}})^{\frac{n}{2}}, \end{aligned}$$

we obtain the formal asymptotic equation for ϕ

$$\begin{aligned} \phi &= 4\pi \left(1 + \left(\frac{1}{3} \mathcal{D}_{\mathbf{x}}^2 - \mathcal{D}_t \right) \varepsilon^2 + \left(\mathcal{D}_t^2 + \frac{1}{5} \mathcal{D}_{\mathbf{x}}^4 - \mathcal{D}_t \mathcal{D}_{\mathbf{x}}^2 \right) \varepsilon^4 \right. \\ &\quad \left. + \left(\frac{1}{7} \mathcal{D}_{\mathbf{x}}^6 + 2\mathcal{D}_t^2 \mathcal{D}_{\mathbf{x}}^2 - \mathcal{D}_t^3 - \mathcal{D}_t \mathcal{D}_{\mathbf{x}}^4 \right) \varepsilon^6 \right) Q + \mathcal{O}(\varepsilon^8). \end{aligned} \quad (2.7)$$

Thus,

$$\begin{aligned} 4\pi Q &= \left(1 + \left(\frac{1}{3} \mathcal{D}_{\mathbf{x}}^2 - \mathcal{D}_t \right) \varepsilon^2 + \left(\mathcal{D}_t^2 + \frac{1}{5} \mathcal{D}_{\mathbf{x}}^4 - \mathcal{D}_t \mathcal{D}_{\mathbf{x}}^2 \right) \varepsilon^4 + \left(\frac{1}{7} \mathcal{D}_{\mathbf{x}}^6 + 2\mathcal{D}_t^2 \mathcal{D}_{\mathbf{x}}^2 - \mathcal{D}_t^3 - \mathcal{D}_t \mathcal{D}_{\mathbf{x}}^4 \right) \varepsilon^6 \right)^{-1} \phi \\ &= \left(1 + \left(-\frac{1}{3} \mathcal{D}_{\mathbf{x}}^2 + \mathcal{D}_t \right) \varepsilon^2 + \left(-\frac{4}{45} \mathcal{D}_{\mathbf{x}}^4 + \frac{1}{3} \mathcal{D}_t \mathcal{D}_{\mathbf{x}}^2 \right) \varepsilon^4 + \left(-\frac{44}{945} \mathcal{D}_{\mathbf{x}}^6 - \frac{1}{3} \mathcal{D}_t^2 \right) \varepsilon^6 \right) \phi + \mathcal{O}(\varepsilon^8). \end{aligned}$$

Substituting the definition of the source term Q from (2.4) in the above equation, yields

$$\begin{aligned} \left(1 - \varepsilon^2 \frac{\sigma_a}{\sigma} \right) \phi + \frac{\varepsilon^2}{\sigma} q &= \left(1 + \left(-\frac{1}{3} \mathcal{D}_{\mathbf{x}}^2 + \mathcal{D}_t \right) \varepsilon^2 + \left(-\frac{4}{45} \mathcal{D}_{\mathbf{x}}^4 + \frac{1}{3} \mathcal{D}_t \mathcal{D}_{\mathbf{x}}^2 \right) \varepsilon^4 \right. \\ &\quad \left. + \left(-\frac{44}{945} \mathcal{D}_{\mathbf{x}}^6 - \frac{1}{3} \mathcal{D}_t^2 \right) \varepsilon^6 \right) \phi + \mathcal{O}(\varepsilon^8). \end{aligned}$$

Multiplying both sides by $\frac{\sigma}{\varepsilon^2}$ and rearranging for ϕ , we obtain

$$-\sigma_a \phi + q = \sigma \mathcal{D}_t \phi - \frac{\sigma}{3} \mathcal{D}_{\mathbf{x}}^2 \left(\phi - \varepsilon^2 \mathcal{D}_t \phi + \frac{4}{15} \varepsilon^2 \mathcal{D}_{\mathbf{x}}^2 \phi + \frac{44}{315} \varepsilon^4 \mathcal{D}_{\mathbf{x}}^4 \phi + \varepsilon^4 \mathcal{D}_t^2 \phi - \frac{4}{5} \varepsilon^4 \mathcal{D}_t \mathcal{D}_{\mathbf{x}}^2 \phi \right) + \mathcal{O}(\varepsilon^6). \quad (2.8)$$

When terms of $\mathcal{O}(\varepsilon^2)$, $\mathcal{O}(\varepsilon^4)$, $\mathcal{O}(\varepsilon^6)$ or $\mathcal{O}(\varepsilon^8)$ are neglected we obtain the simplified P_0 , P_1 , P_2 or P_3 approximations, respectively. Higher order approximations can be derived in a similar manner. In the current study, we consider only the simplified P_1 approximation and the extension of our frequency-domain method to the other approximations is straightforward. Hence, neglecting the terms of order $\mathcal{O}(\varepsilon^2)$ in (2.8), one obtains the simplified P_1 approximation

$$-\sigma_a \phi + q = \sigma \mathcal{D}_t \phi - \frac{\sigma}{3} \mathcal{D}_{\mathbf{x}}^2 \phi,$$

which is equivalent to

$$\frac{\varepsilon^2}{\mathcal{V}} \frac{\partial \phi}{\partial t}(t, \mathbf{x}) - \frac{\varepsilon^2}{3\sigma} \nabla^2 \phi(t, \mathbf{x}) + \sigma_a \phi(t, \mathbf{x}) = q(t, \mathbf{x}), \quad (t, \mathbf{x}) \in (0, T] \times \Omega. \quad (2.9)$$

The boundary conditions for simplified P_N approximations are derived from variational principles and are strongly connected to the Marshak conditions for the P_N approximations, compare [22]. Here we formulate boundary conditions for the simplified P_1 approximation which are consistent with radiative boundary conditions (2.2). For more general formulation of these boundary conditions we refer the reader to [17]. Hence, the boundary conditions for the simplified P_1 equation (2.9) are

$$\frac{2\varepsilon}{3\sigma} \mathbf{n}(\xi) \cdot \nabla \phi(t, \xi) + \phi(t, \xi) = g(t, \xi), \quad (t, \xi) \in (0, T] \times \Gamma, \quad (2.10)$$

where

$$g(t, \xi) = -4 \int_{\mathbb{S}^2} \psi_b(t, \xi, \hat{\mathbf{s}}) d\hat{\mathbf{s}}, \quad (t, \xi) \in (0, T] \times \Gamma^-.$$

A consistent initial condition for (2.9) can be derived from the initial condition (2.3) as

$$\phi(0, \mathbf{x}) = \phi_0(\mathbf{x}) := \int_{\mathbb{S}^2} \psi_0(\mathbf{x}, \hat{\mathbf{s}}) d\hat{\mathbf{s}}, \quad \mathbf{x} \in \Omega. \quad (2.11)$$

Note that the asymptotic analysis presented in the present work can be generalized for anisotropic scattering cases using similar techniques as those proposed in [9] for the steady-state radiative transfer equations. Thus, in non-homogeneous anisotropic media, the full radiative transfer problem (2.1)-(2.3) is replaced by the following parabolic problem

$$\begin{aligned} \frac{\varepsilon^2}{\mathcal{V}} \frac{\partial \phi}{\partial t} - \nabla \cdot \left(\frac{\varepsilon^2}{3\sigma(\mathbf{x})} \nabla \phi(t, \mathbf{x}) \right) + \sigma_a(\mathbf{x}) \phi(t, \mathbf{x}) &= q(t, \mathbf{x}), & (t, \mathbf{x}) \in (0, T] \times \Omega, \\ \frac{2\varepsilon}{3\sigma(\xi)} \mathbf{n}(\xi) \cdot \nabla \phi(t, \xi) + \phi(t, \xi) &= g(t, \xi), & (t, \xi) \in (0, T] \times \partial\Omega, \\ \phi(0, \mathbf{x}) &= \phi_0(\mathbf{x}), & \mathbf{x} \in \Omega. \end{aligned} \quad (2.12)$$

It should be stressed that the diffusion scale ε in (2.12) depends on the optical characteristics of the media and the reference thickness of the medium. It is used to differentiate between an optically thick medium (small values of ε) and optically thin medium (large values of ε).

3 Frequency-domain Approach

In the sequel, we use the following notations. The classical space $L^2(\Omega, \mathbb{C})$ of square integrable complex-valued functions on the domain Ω is denoted by $\widehat{L}_2 := L^2(\Omega, \mathbb{C})$. The space \widehat{L}_2 is endowed by its natural topology defined by the following inner product and its associated norm

$$(u|v)_2 = \int_{\Omega} u(x) \overline{v(x)} dx, \quad \|u\|_2 = \sqrt{(u|u)_2}, \quad \forall u, v \in \widehat{L}_2.$$

For every $k \in \mathbb{N}$, let $\widehat{\mathbf{H}}_k = \mathbf{H}^k(\Omega, \mathbb{C}) := \mathbf{W}^{k,2}(\Omega, \mathbb{C})$ be the usual Sobolev space, with the classical norm $\|\cdot\|_{\widehat{\mathbf{H}}_k}$ given by

$$\|u\|_{\widehat{\mathbf{H}}_k} = \left(\sum_{|\ell| \leq k} \|\partial^\ell u\|_2^2 \right)^{\frac{1}{2}}, \quad \forall u \in \widehat{\mathbf{H}}_k, \quad (3.1)$$

where $\partial^\ell u := \partial^{\ell_1} \dots \partial^{\ell_d} u$ stands for the derivative, in the distribution sense, of u of order $|\ell| = \sum_{i=1}^d \ell_i$ and $\partial^{\ell_i} = \frac{\partial^{\ell_i}}{\partial x^{\ell_i}}$, for $i = 1, \dots, d$. The classical space $L^2(\Omega, \mathbb{R})$ of square integrable real-valued functions on the domain Ω is denoted by $L_2 := L^2(\Omega, \mathbb{R})$ and \mathbf{H}_k denotes the usual Sobolev space of real-valued functions defined by $\mathbf{H}_k = \mathbf{H}^k(\Omega, \mathbb{R}) := \mathbf{W}^{k,2}(\Omega, \mathbb{R})$. The space \mathbf{H}_k is equipped with the classical norm $\|\cdot\|_{\mathbf{H}_k}$ given in (3.1).

We assume that, the mean radiative intensity $t \mapsto \phi(t, \mathbf{x})$ and the gradient derivative function $t \mapsto \nabla^2 \phi(t, \mathbf{x})$ has extensions to \mathbb{R} which belong to the space $L^1(\mathbb{R}, \mathbb{R})$, almost everywhere in Ω . We also assume that the given source term q and boundary function g have extensions, still denoted by q and g , such that $q \in L^\infty(\Omega; L^1(\mathbb{R}, \mathbb{R}))$ and $g \in L^\infty(\partial\Omega; L^1(\mathbb{R}, \mathbb{R}))$. Recall that the Fourier transform $\widehat{\psi}$ of a function ψ in $L^1(\mathbb{R}, \mathbb{R})$ is given by

$$\widehat{\psi}(\omega) = \frac{1}{\sqrt{2\pi}} \int_{-\infty}^{+\infty} \psi(t) e^{-i\omega t} dt, \quad i = \sqrt{-1}. \quad (3.2)$$

By using the well-established Lebesgue theorem of differentiation under the integral form, we obtain

$$\widehat{\nabla^2 \phi}(\omega, \mathbf{x}) = \nabla^2 \widehat{\phi}(\omega, \mathbf{x}), \quad \forall (\omega, \mathbf{x}) \in \mathbb{R} \times \Omega. \quad (3.3)$$

In this section we apply the Fourier transform to the parabolic simplified P_1 problem (2.12). By using the classical relation $\frac{\partial \widehat{\psi}}{\partial t} = i\omega \widehat{\psi}$ and the equation (3.3) one obtains the following elliptic simplified P_1 problem to be solved in the frequency domain for the radiative density u as

$$\begin{aligned} -\nabla \cdot \left(\frac{\varepsilon^2}{3\sigma(\mathbf{x})} \nabla u(\omega, \mathbf{x}) \right) + \left(\sigma_a(\mathbf{x}) + \frac{i\omega \varepsilon^2}{\mathcal{V}} \right) u(\omega, \mathbf{x}) &= F(\omega, \mathbf{x}), & (\omega, \mathbf{x}) \in \mathbb{R} \times \Omega, \\ \frac{2\varepsilon}{3\sigma(\xi)} \mathbf{n}(\xi) \cdot \nabla u(\omega, \xi) + u(\omega, \xi) &= G(\omega, \xi), & (\omega, \xi) \in \mathbb{R} \times \partial\Omega, \end{aligned} \quad (3.4)$$

where $u(\omega, \cdot) = \widehat{\phi}(\omega, \cdot)$, $F(\omega, \cdot) = \widehat{q}(\omega, \cdot)$ and $G(\omega, \cdot) = \widehat{g}(\omega, \cdot)$ are the Fourier transforms with respect to the time variable t of $\phi(\cdot, \mathbf{x})$, $q(\cdot, \mathbf{x})$ and $g(\cdot, \xi)$, respectively.

3.1 The variational formulation

Let $u_*(\omega, \cdot) \in \widehat{\mathbf{H}}_1$ be a sufficiently smooth function satisfying the problem (3.4). Multiplying the simplified P_1 equation in the frequency-domain by an arbitrary function $\bar{v} \in \widehat{\mathbf{H}}_1$, and integrating over Ω by using the Green-Gauss formula with respect to the non-homogeneous boundary conditions, provides the weak variational formulation

$$\mathcal{A}_\omega(u_*(\cdot, \omega), v) = \mathcal{L}_\omega(v), \quad \forall v \in \widehat{\mathbf{H}}_1, \quad (3.5)$$

where the sesquilinear form $\mathcal{A}_\omega : \widehat{\mathbf{H}}_1 \times \widehat{\mathbf{H}}_1 \rightarrow \mathbb{C}$ and the semi-linear form $\mathcal{L}_\omega : \widehat{\mathbf{H}}_1 \rightarrow \mathbb{C}$ are defined for all $u, v \in \widehat{\mathbf{H}}_1$ by

$$\mathcal{A}_\omega(u, v) = \int_\Omega \frac{\varepsilon^2}{3\sigma(\mathbf{x})} \nabla u(\mathbf{x}) \overline{\nabla v(\mathbf{x})} d\mathbf{x} + \int_\Omega \left(\sigma_a(\mathbf{x}) + \frac{i\omega \varepsilon^2}{\mathcal{V}} \right) u(\mathbf{x}) \overline{v(\mathbf{x})} d\mathbf{x} + \frac{\varepsilon}{2} \int_{\partial\Omega} u(\xi) \overline{v(\xi)} d\mu(\xi), \quad (3.6)$$

and

$$\mathcal{L}_\omega(v) = \frac{\varepsilon}{2} \int_{\partial\Omega} G(\omega, \xi) \overline{v(\xi)} d\mu(\xi) + \int_\Omega F(\omega, \mathbf{x}) \overline{v(\mathbf{x})} d\mathbf{x}, \quad (3.7)$$

respectively. Here, $d\mu$ is the measure of unit area on the boundary $\partial\Omega$. It has been shown in [2, 3] that the variational problem (3.5) is equivalent to the frequency-domain problem (3.4). From the trace theorem, there exists a constant $C > 0$ (depending only on Ω) such that

$$\|u\|_{L^2(\partial\Omega, \mathbb{C})} \leq C \|u\|_{\widehat{\mathbf{H}}_1}, \quad \forall u \in \widehat{\mathbf{H}}_1. \quad (3.8)$$

Using the Schwarz inequality and the Sobolev continuous embedding theorem, it follows that there exists a constant $C_0 > 0$ (depending on $\partial\Omega$) such that

$$|\mathcal{L}_\omega(v)| \leq M(\omega) \|v\|_{\widehat{\mathbf{H}}_1}, \quad \forall v \in \widehat{\mathbf{H}}_1, \quad (3.9)$$

where

$$M(\omega) = C_0 \left(\|F(\omega, \cdot)\|_{\widehat{\mathbf{L}}_2} + \|G(\omega, \cdot)\|_{L^2(\partial\Omega, \mathbb{C})} \right). \quad (3.10)$$

Therefore, \mathcal{L}_ω is a continuous semi-linear operator on $\widehat{\mathbf{H}}_1$. Using the Sobolev continuous embedding theorem, there exists a nonnegative constant C_1 not depending on the frequency ω such that

$$|\mathcal{A}_\omega(u, v)| \leq C_1 \sqrt{1 + \omega^2} \|u\|_{\widehat{\mathbf{H}}_1} \|v\|_{\widehat{\mathbf{H}}_1}, \quad \forall (u, v) \in \widehat{\mathbf{H}}_1 \times \widehat{\mathbf{H}}_1. \quad (3.11)$$

It is obvious to obtain the coercivity bound

$$\operatorname{Re}(\mathcal{A}_\omega(u, u)) \geq \alpha \|u\|_{\widehat{\mathbf{H}}_1}^2, \quad \forall u \in \widehat{\mathbf{H}}_1, \quad (3.12)$$

where $\operatorname{Re}(\mathcal{A})$ denote the real part of \mathcal{A} and α is a positive constant given by

$$\alpha = \min \left(\frac{\varepsilon^2}{3\sigma}, \sigma_a \right). \quad (3.13)$$

Hence, from (3.11) and (3.12), the sesquilinear form \mathcal{A}_ω is continuous and coercive. Let us recall the following theorem established in [2, 3].

Theorem 3.1 *For a fix frequency ω in \mathbb{R} , the problem (3.4) has a unique solution $u_*(\cdot, \omega)$ in $\widehat{\mathbf{H}}_2$ satisfying*

$$\|u_*(\cdot, \omega)\|_{\widehat{\mathbf{H}}_1} \leq \frac{M(\omega)}{\alpha}, \quad (3.14)$$

where α and $M(\omega)$ are defined in (3.10) and (3.13), respectively. Furthermore, if the function $F(\cdot, \omega)$ is in $\mathcal{C}(\overline{\Omega})$, then $u_*(\cdot, \omega) \in \mathcal{C}^2(\overline{\Omega})$ is the unique solution of the problem (3.4) in the usual sense.

3.2 Tensor-product spline Galerkin approximation

We assume without loss of generality, a two-dimensional rectangular domain $\overline{\Omega} = [a, b] \times [c, d]$, covered with a uniform numerical mesh defined by

$$\Omega_h = \left\{ \mathbf{x}_{i,j} = (x_i, y_j)^T, \quad x_i = a + ih_1, \quad y_j = c + jh_2, \quad i = 0, 1, \dots, I, \quad j = 0, 1, \dots, J \right\},$$

where $h_1 = \frac{b-a}{I}$, $h_2 = \frac{d-c}{J}$ and h denotes the maximum cell size, $h = \max(h_1, h_2)$. For a fixed frequency ω in \mathbb{R} , let us denote by $\widehat{\mathbf{V}}_h$ the finite dimensional subspace of $\widehat{\mathbf{H}}_2$ given by

$$\widehat{\mathbf{V}}_h = \left\{ u_h(\omega, \cdot) \in \widehat{\mathbf{H}}_2 : u_h(\cdot, \omega) \Big|_{\mathcal{C}_{ij}} \in \mathbb{P}_3(\Omega); \quad \text{for } 0 \leq i \leq I-1, \quad 0 \leq j \leq J-1 \right\},$$

where $\mathcal{C}_{ij} = [x_i, x_{i+1}] \times [y_j, y_{j+1}]$ is the mesh cell in Ω_h and $\mathbb{P}_3(\Omega)$ is the space of polynomials on Ω of degree ≤ 3 . It is obvious that the dimension of the subspace $\widehat{\mathbf{V}}_h$ is $N = N_1 \times N_2$, with $N_1 = I+3$ and $N_2 = J+3$.

We use the classical cubic B-spline (B_{ij}) as a basis of the subspace $\widehat{\mathbb{V}}_h$. Here, $(B_{ij})_{\substack{1 \leq i \leq N_1 \\ 1 \leq j \leq N_2}}$ denotes the tensor-product B-splines associated with the mesh cell \mathcal{C}_{ij} . For $i = 1, \dots, N_1$ and $j = 1, \dots, N_2$, we have

$$B_{ij}(x, y) = B_i(x)B_j(y),$$

where

$$B_i(x) = \mathcal{B}_3\left(\frac{x - x_{i-4}}{h_1}\right) \quad \text{and} \quad B_j(y) = \mathcal{B}_3\left(\frac{y - y_{j-4}}{h_2}\right), \quad (3.15)$$

with \mathcal{B}_3 is a cubic B-spline with the support embedded in $[0, 4]$, see for example [2, 3].

The classical Galerkin approximation consists of finding an approximation $u_{*h}(\omega, \cdot)$ of the exact solution $u_*(\omega, \cdot)$ as a solution in $\widehat{\mathbb{V}}_h$ of the following discrete variational problem

$$\mathcal{A}_\omega(u_h(\omega, \cdot), v_h) = \mathcal{L}_\omega(v_h), \quad \forall v_h \in \widehat{\mathbb{V}}_h, \quad (3.16)$$

where \mathcal{A}_ω and \mathcal{L}_ω are given in (3.6) and (3.7), respectively. The solution $u_{*h}(\omega, \cdot)$ of the problem (3.16) is written in the following form

$$u_h(\omega, x, y) = \sum_{i=1}^{N_1} \sum_{j=1}^{N_2} Z_{h,ij}(\omega) B_{ij}(x, y), \quad \forall (x, y) \in \overline{\Omega}, \quad (3.17)$$

where $Z_{h,ij}(\omega)$ are complex coefficients. By using the test function $v_h(x, y) = B_{kl}(x, y)$ on the weak variational formulation (3.5) or (3.16), we obtain the Galerkin approximation

$$\sum_{i=1}^{N_1} \sum_{j=1}^{N_2} Z_{h,ij}(\omega) A_{ijkl}(\omega) = \mathcal{L}_\omega(B_{kl}), \quad (3.18)$$

where

$$\begin{aligned} A_{ijkl}(\omega) &= \int_{\Omega} \frac{\varepsilon^2}{3\sigma(x, y)} (\nabla B_{ij})(x, y) (\nabla B_{kl})(x, y) dx dy + \frac{\varepsilon}{2} \int_{\partial\Omega} B_{ij}(x, y) B_{kl}(x, y) d\mu(x, y) \\ &+ \int_{\Omega} \left(\sigma_a(x, y) + \frac{i\omega\varepsilon^2}{\nu} \right) B_{ij}(x, y) B_{kl}(x, y) dx dy, \end{aligned}$$

and

$$\mathcal{L}_\omega(B_{kl}) = \frac{\varepsilon}{2} \int_{\partial\Omega} G(\omega, x, y) B_{kl}(x, y) d\mu(x, y) + \int_{\Omega} F(\omega, x, y) B_{kl}(x, y) dx dy,$$

for $i, k = 1, \dots, N_1$ and $j, \ell = 1, \dots, N_2$. In order to formulate the problem in a matrix form we define the $N_1 N_2 \times N_1 N_2$ matrix $A(\omega) = [A_{ijkl}(\omega)]$ the entries of which are the complex coefficients $A_{ijkl}(\omega) = \mathcal{A}_\omega(B_{ij}, B_{kl})$, the $N_1 \times N_2$ matrix $\mathbf{B}_h(\omega) = [\mathbf{B}_{h,kl}(\omega)]$ the entries of which are $\mathbf{B}_{h,kl}(\omega) = \mathcal{L}_\omega(B_{kl})$ and the $N_1 \times N_2$ matrix $\mathbf{Z}_h(\omega) = [Z_{h,ij}(\omega)]$ the entries of which are unknown complex coefficients. We also define the $N_1 N_2$ vectors $\mathbf{b}_h(\omega)$ and $\mathbf{z}_h(\omega)$ the entries of which are the complex coefficients $\mathbf{B}_h(\omega)$ and $\mathbf{Z}_h(\omega)$, respectively. Hence, the relations (3.18) lead to the following $N_1 N_2 \times N_1 N_2$ linear system

$$A(\omega) \mathbf{z}_h(\omega) = \mathbf{b}_h(\omega), \quad (3.19)$$

where for all frequency values ω , the entries $Z_{h,ij}(\omega)$ appearing in the expression (3.17) of the approximate solution u_{*h} are obtained by solving the linear system (3.19). The coefficients of the matrix $A(\omega)$ are defined as

$$A_{ijkl}(\omega) = \frac{\varepsilon^2}{3} D_{ijkl} + U_{ijkl} + \frac{\varepsilon}{2} Q_{ijkl} + \frac{i\omega\varepsilon^2}{\nu} C_{ijkl},$$

where the coefficients D_{ijkl} , U_{ijkl} , Q_{ijkl} and C_{ijkl} are given by

$$\begin{aligned} D_{ijkl} &= \frac{1}{h_1^2} \int_{\Omega} \frac{1}{\sigma(x, y)} B'_i(x) B_j(y) B'_k(x) B_\ell(y) dx dy + \frac{1}{h_2^2} \int_{\Omega} \frac{1}{\sigma(x, y)} B_i(x) B'_j(y) B_k(x) B'_\ell(y) dx dy, \\ U_{ijkl} &= \int_{\Omega} \sigma_a(x, y) B_i(x) B_j(y) B_k(x) B_\ell(y) dx dy, \\ Q_{ijkl} &= \int_{\partial\Omega} B_i(x) B_j(y) B_k(x) B_\ell(y) d\mu(x, y), \\ C_{ijkl} &= \int_{\Omega} B_i(x) B_j(y) B_k(x) B_\ell(y) dx dy. \end{aligned}$$

Note that in most radiative transfer applications the absorption and scattering coefficients are assumed to be either homogeneous constants or piecewise constants in the considered computational domain. In both cases and many other situations, a variable separation can be used to decompose these coefficients. In the present study we assume that

$$\sigma(x, y) = \sigma_1(x)\sigma_2(y), \quad \sigma_a(x, y) = \sigma_{a1}(x)\sigma_{a2}(y).$$

Hence, by using the expressions of B_i and B_j given in (3.15) and by introducing the variables $s \in [0, I]$ and $\tau \in [0, J]$ such that $x = a + sh_1$ and $y = c + \tau h_2$, we obtain

$$\begin{aligned} D_{ijkl} &= \frac{h_2}{h_1} \int_0^J \int_0^I \frac{1}{\sigma(a + sh_1, c + \tau h_2)} \mathcal{B}_3(\tau - j + 4) \mathcal{B}_3(\tau - \ell + 4) \mathcal{B}'_3(s - i + 4) \mathcal{B}'_3(s - k + 4) ds d\tau + \\ &\quad \frac{h_1}{h_2} \int_0^J \int_0^I \frac{1}{\sigma(a + sh_1, c + \tau h_2)} \mathcal{B}'_3(\tau - j + 4) \mathcal{B}'_3(\tau - \ell + 4) \mathcal{B}_3(s - i + 4) \mathcal{B}_3(s - k + 4) ds d\tau, \\ U_{ijkl} &= h_1 h_2 \int_0^J \int_0^I \sigma_a(a + sh_1, c + \tau h_2) \mathcal{B}_3(\tau - j + 4) \mathcal{B}_3(\tau - \ell + 4) \mathcal{B}_3(s - i + 4) \mathcal{B}_3(s - k + 4) ds d\tau, \\ C_{ijkl} &= h_1 h_2 \int_0^J \int_0^I \mathcal{B}_3(\tau - j + 4) \mathcal{B}_3(\tau - \ell + 4) \mathcal{B}_3(s - i + 4) \mathcal{B}_3(s - k + 4) ds d\tau, \end{aligned}$$

and

$$\begin{aligned} Q_{ijkl} &= h_2 \mathcal{B}_3(-i + 4) \mathcal{B}_3(-k + 4) \int_0^J \mathcal{B}_3(\tau - j + 4) \mathcal{B}_3(\tau - \ell + 4) d\tau + \\ &\quad h_2 \mathcal{B}_3(I - i + 4) \mathcal{B}_3(I - k + 4) \int_0^J \mathcal{B}_3(\tau - j + 4) \mathcal{B}_3(\tau - \ell + 4) d\tau + \\ &\quad h_1 \mathcal{B}_3(-j + 4) \mathcal{B}_3(-\ell + 4) \int_0^I \mathcal{B}_3(s - i + 4) \mathcal{B}_3(s - k + 4) ds + \\ &\quad h_1 \mathcal{B}_3(J - j + 4) \mathcal{B}_3(J - \ell + 4) \int_0^I \mathcal{B}_3(s - i + 4) \mathcal{B}_3(s - k + 4) ds + \\ &\quad \mathcal{B}_3(-i + 4) \mathcal{B}_3(-k + 4) \mathcal{B}_3(-j + 4) \mathcal{B}_3(-\ell + 4) + \\ &\quad \mathcal{B}_3(-i + 4) \mathcal{B}_3(-k + 4) \mathcal{B}_3(J - j + 4) \mathcal{B}_3(J - \ell + 4) + \\ &\quad \mathcal{B}_3(I - i + 4) \mathcal{B}_3(I - k + 4) \mathcal{B}_3(-j + 4) \mathcal{B}_3(-\ell + 4) + \\ &\quad \mathcal{B}_3(I - i + 4) \mathcal{B}_3(I - k + 4) \mathcal{B}_3(J - j + 4) \mathcal{B}_3(J - \ell + 4). \end{aligned}$$

The weight matrix $A(\omega)$ is given by

$$A(\omega) = \frac{\varepsilon^2}{3} M_\sigma + M_{\sigma_a} + \frac{i\omega\varepsilon^2}{\mathcal{V}} M_\nu + \frac{\varepsilon}{2} M_{\partial\Omega},$$

where the matrices M_σ , M_{σ_a} , M_ν and $M_{\partial\Omega}$ can be decomposed respectively as a sum of Kronecker products as follows:

$$\begin{aligned} M_\sigma &= \frac{h_2}{h_1} D_2^{0T} \otimes D_1^{1T} + \frac{h_1}{h_2} D_2^{1T} \otimes D_1^{0T}, \\ M_{\sigma_a} &= h_1 h_2 U_2^T \otimes U_1^T, \\ M_\nu &= h_1 h_2 C_2^T \otimes C_1^T, \\ M_{\partial\Omega} &= h_1 \left(\Gamma^{(2,0)} + \Gamma^{(2,1)} \right)^T \otimes \Lambda_1^T + h_2 \Lambda_2^T \otimes \left(\Gamma^{(1,0)} + \Gamma^{(1,1)} \right)^T + \\ &\quad \Gamma^{(2,1)T} \otimes \left(\Gamma^{(1,0)} + \Gamma^{(1,1)} \right)^T + \Gamma^{(2,0)T} \otimes \left(\Gamma^{(1,0)} + \Gamma^{(1,1)} \right)^T, \end{aligned}$$

with the entries of the matrices M_σ are

$$\begin{aligned} D_1^\ell(i, k) &= \int_0^I \frac{1}{\sigma_1(a + sh_1)} \mathcal{B}_3^{(\ell)}(s - i + 4) \mathcal{B}_3^{(\ell)}(s - k + 4) ds, \\ D_2^\ell(j, l) &= \int_0^J \frac{1}{\sigma_2(c + \tau h_2)} \mathcal{B}_3^{(\ell)}(\tau - j + 4) \mathcal{B}_3^{(\ell)}(\tau - l + 4) d\tau, \quad \ell = 0, 1. \end{aligned}$$

Here, $\mathcal{B}_3^{(\ell)}$ is the ℓ th derivative of the cubic B-spline. The components of M_{σ_a} are

$$\begin{aligned} U_1(i, k) &= \int_0^I \sigma_{a1}(a + sh_1) \mathcal{B}_3(s - i + 4) \mathcal{B}_3(s - k + 4) ds, \\ U_2(j, l) &= \int_0^J \sigma_{a2}(c + \tau h_2) \mathcal{B}_3(\tau - j + 4) \mathcal{B}_3(\tau - l + 4) d\tau, \end{aligned}$$

the components of M_ν are

$$\begin{aligned} C_1(i, k) &= \int_0^I \mathcal{B}_3(s - i + 4) \mathcal{B}_3(s - k + 4) ds, \\ C_2(j, l) &= \int_0^J \mathcal{B}_3(\tau - j + 4) \mathcal{B}_3(\tau - l + 4) d\tau, \end{aligned}$$

and the components of the matrices $M_{\partial\Omega}$ are

$$\begin{aligned} \Lambda_1(i, k) &= \int_0^I \mathcal{B}_3(s - i + 4) \mathcal{B}_3(s - k + 4) ds, \\ \Lambda_2(j, l) &= \int_0^J \mathcal{B}_3(\tau - j + 4) \mathcal{B}_3(\tau - l + 4) d\tau, \end{aligned}$$

$$\Gamma^{(2,0)}(j, l) = \mathcal{B}_3(-j + 4) \mathcal{B}_3(-l + 4), \quad \Gamma^{(2,1)}(j, l) = \mathcal{B}_3(J - j + 4) \mathcal{B}_3(J - l + 4),$$

$$\Gamma^{(1,0)}(i, k) = \mathcal{B}_3(-i + 4) \mathcal{B}_3(-k + 4), \quad \Gamma^{(1,1)}(i, k) = \mathcal{B}_3(I - i + 4) \mathcal{B}_3(I - k + 4).$$

Finally, the coefficients $\mathbf{B}_{h,kl}(\omega)$ in the matrix of the source term are given by

$$\mathbf{B}_{h,kl}(\omega) = \frac{\varepsilon}{2} \int_{\partial\Omega} G(\omega, x, y) B_{k\ell}(x, y) d\mu(x, y) + \int_{\Omega} F(\omega, x, y) B_{k\ell}(x, y) dx dy.$$

We also use similar techniques as above to obtain

$$\begin{aligned}
F_{h,k\ell}(\omega) &= h_1 h_2 \int_0^J \int_0^I F(\omega, a + sh_1, c + \tau h_2) \mathcal{B}_3(s - k + 4) \mathcal{B}_3(\tau - \ell + 4) ds d\tau, \\
G_{h,k\ell}(\omega) &= h_2 \mathcal{B}_3(-k + 4) \int_0^J G(\omega, a, c + h_2 \tau) \mathcal{B}_3(\tau - \ell + 4) d\tau + \\
&\quad h_2 \mathcal{B}_3(I - k + 4) \int_0^J G(\omega, b, c + h_2 \tau) \mathcal{B}_3(\tau - \ell + 4) d\tau + \\
&\quad h_1 \mathcal{B}_3(-\ell + 4) \int_0^I G(\omega, a + h_1 s, c) \mathcal{B}_3(s - k + 4) ds + \\
&\quad h_1 \mathcal{B}_3(J - \ell + 4) \int_0^I G(\omega, a + h_1 s, d) \mathcal{B}_3(s - k + 4) ds + \\
&\quad \mathcal{B}_3(-\ell + 4) \left(G(\omega, a, c) \mathcal{B}_3(-k + 4) + G(\omega, b, c) \mathcal{B}_3(I - k + 4) \right) + \\
&\quad \mathcal{B}_3(J - \ell + 4) \left(G(\omega, a, d) \mathcal{B}_3(-k + 4) + G(\omega, b, d) \mathcal{B}_3(I - k + 4) \right).
\end{aligned}$$

Thus, the coefficients $\mathbf{B}_{h,k\ell}(\omega)$ are given by

$$\mathbf{B}_{h,k\ell}(\omega) = \frac{\varepsilon}{2} G_{h,k\ell}(\omega) + F_{h,k\ell}(\omega), \quad k = 1, \dots, N_1, \quad \ell = 1, \dots, N_2.$$

It should be stressed that our method for the simplified P_1 is to solve the system (3.18) in the frequency-space domain for a discrete set of frequencies ω of interest, and then to take the discrete inverse Fourier transforms in order to obtain the approximate solutions in the time-space domain. Apparently, the proposed method is a natural parallel algorithm which does not require any significant communication costs among processors, since solving the system (3.18) for each frequency is independent of solving (3.18) for other frequencies.

4 Solution of the inverse Fourier transform

In this section, an approximate solution ϕ_{*h} of the exact solution ϕ_* is obtained as the inverse Fourier transform of u_{*h} . Therefore, we will use the Gauss-Hermite quadrature formulation to compute the inverse Fourier transform of u_{*h} . We have the following result:

Theorem 4.1 *For every fixed time t , the problem (2.12) has a unique solution $\phi_*(t, \cdot)$ obtained as the inverse Fourier transform of the unique solution $u_*(\omega, \cdot)$ of the problem (3.4) and it is given by*

$$\phi_*(t, x, y) = \frac{1}{\sqrt{2\pi}} \int_{-\infty}^{+\infty} u_*(\omega, x, y) e^{it\omega} d\omega, \quad \forall (x, y) \in \bar{\Omega}. \quad (4.1)$$

Furthermore, the solution $\phi_*(t, \cdot)$ belongs to the space H_2 .

We skip the proof of these classical results, see for instance [7, 2] for further details. An approximate solution $\phi_{*h}(t, x, y)$ of the problem (2.12) is obtained by using the inverse Fourier transform as in (4.1),

$$\phi_{*h}(t, x, y) = \frac{1}{\sqrt{2\pi}} \int_{-\infty}^{+\infty} u_{*h}(\omega, x, y) e^{it\omega} d\omega.$$

Consider the finite-dimensional vector space \mathbb{V}_h with dimension N given by

$$\mathbb{V}_h = \left\{ \phi_h \in H_2 : \phi_h|_{c_{ij}} \in \mathbb{P}_3(\Omega); \quad \text{for } 0 \leq i \leq I - 1, 0 \leq j \leq J - 1 \right\}.$$

The approximate solution $\phi_{*h}(t, \cdot, \cdot)$ is an element of the space \mathbb{V}_h and it is given by

$$\phi_{*h}(t, x, y) = \sum_{i=1}^{N_1} \sum_{j=1}^{N_2} \mathbb{V}_{h,ij}(t) B_{ij}(x, y), \quad \forall (x, y) \in \bar{\Omega}, \quad (4.2)$$

where the functions

$$\mathbb{V}_{h,ij}(t) = \int_{-\infty}^{+\infty} \mathbb{Z}_{h,ij}(\omega) e^{it\omega} d\omega,$$

are the inverse Fourier transforms of the functions $\mathbb{Z}_{h,ij}$ given in (3.17). Let us define the functions

$$\chi_{ij}(\omega, t) = \frac{1}{\sqrt{2\pi}} e^{(\omega^2 + it\omega)} \mathbb{Z}_{h,ij}(\omega),$$

then,

$$\mathbb{V}_{h,ij}(t) = \int_{-\infty}^{+\infty} \chi_{ij}(\omega, t) e^{-\omega^2} d\omega, \quad 1 \leq i \leq N_1, \quad 1 \leq j \leq N_2. \quad (4.3)$$

To compute the integral given by (4.3), we use the Gauss-Hermite quadrature formula

$$\int_{-\infty}^{+\infty} \chi_{ij}(\omega, t) e^{-\omega^2} d\omega \simeq \sum_{\ell=0}^m \alpha_\ell \chi_{ij}(\omega_\ell, t),$$

where the nodal points $(\omega_\ell)_{0 \leq \ell \leq m}$ are the zeros of the Hermite polynomial H_{m+1} of degree $m+1$, and the weight coefficients $(\alpha_\ell)_{0 \leq \ell \leq m}$ are given by the Christoffel-Darboux formula [1, 3],

$$\alpha_\ell = \frac{1}{H'_{m+1}(\omega_\ell)} \int_{-\infty}^{+\infty} \frac{H_{m+1}(\omega)}{\omega - \omega_\ell} e^{-\omega^2} d\omega = \frac{2^m m! \sqrt{\pi}}{(m+1)[H_m(\omega_\ell)]^2}.$$

Thus, the coefficients $\mathbb{V}_{h,ij}(t)$ given in (4.3) are approximated as follows

$$\mathbb{V}_{h,ij}(t) \simeq \sum_{\ell=0}^m \alpha_\ell \chi_{ij}(\omega_\ell, t), \quad 1 \leq i \leq N_1, \quad 1 \leq j \leq N_2. \quad (4.4)$$

Finally, using (4.2) and (4.4), we get

$$\phi_{*h}(t, x, y) \simeq \sum_{i=1}^{N_1} \sum_{j=1}^{N_2} \left(\sum_{\ell=0}^m \alpha_\ell \chi_{ij}(\omega_\ell, t) \right) B_{ij}(x, y) = \sum_{\ell=0}^m \alpha_\ell \left(\sum_{i=1}^{N_1} \sum_{j=1}^{N_2} \chi_{ij}(\omega_\ell, t) B_{ij}(x, y) \right).$$

In summary, the proposed frequency-domain procedure to solve the simplified P₁ problem (2.12) can be carried out in the following two steps:

1. Forward stage:

1.1. Construct the Fourier transforms $u(\omega, \cdot) = \widehat{\phi}(\omega, \cdot)$, $F(\omega, \cdot) = \widehat{q}(\omega, \cdot)$ and $G(\omega, \cdot) = \widehat{g}(\omega, \cdot)$ of $\phi(\cdot, \mathbf{x})$, $q(\cdot, \mathbf{x})$ and $g(\cdot, \xi)$ according to (3.2).

1.2. For each frequency ω :

i. Form the tensor-product spline basis $B_{ij}(x, y) = B_i(x)B_j(y)$ such that

$$u_h(\omega, x, y) = \sum_{i=1}^{N_1} \sum_{j=1}^{N_2} \mathbb{Z}_{h,ij}(\omega) B_{ij}(x, y).$$

ii. Formulate the weak variational formulation

$$\mathcal{A}_\omega(u_h(\omega, \cdot), B_{k\ell}) = \mathcal{L}_\omega(B_{k\ell}).$$

iii. Solve the linear system

$$A(\omega)z_h(\omega) = b_h(\omega).$$

2. Backward stage:

2.1. Using the inverse Fourier transform and the Gauss-Hermite quadrature method, calculate

$$V_{h,ij}(t) = \frac{1}{\sqrt{2\pi}} \sum_{\ell=0}^m \alpha_\ell e^{(\omega_\ell^2 + it\omega_\ell)} Z_{h,ij}(\omega_\ell),$$

for $i = 1, \dots, N_1$ and $j = 1, \dots, N_2$.

2.2. For a fixed time $t \in [0, T]$, compute the solution

$$\phi_h(t, x, y) = \sum_{i=1}^{N_1} \sum_{j=1}^{N_2} V_{h,ij}(t) B_{ij}(x, y).$$

In the current study, the resulting linear systems of algebraic equations in (3.19) are solved using a direct solver. It should be pointed out that the conditioning issue usually attributed to the frequency-domain techniques are also present in the proposed approach. However, a direct solver using double precision was found to produce results of suitable accuracy in the linear system computations presented in this paper. For larger systems than those considered here an iterative solver might become preferable.

5 Numerical results and applications

Several test problems are considered to demonstrate the performance of the proposed frequency-domain method. We consider examples in radiative transfer with scattering and absorption coefficients either constant or depending on the space variable. In order to show the merits of the proposed method, the comparisons among the new approach and the radiative transfer simulation is also carried out. In addition, the examination of the computational cost is performed to evaluate the efficiency of the method. For comparison reasons we also solve the simplified P_1 problem (2.12) in the time domain using finite difference techniques for the space discretization. We define a regular mesh over Ω with gridpoints $\mathbf{x}_{i,j} = (x_i, y_j)$ and spatial scales Δx and Δy in x - and y -direction, respectively. Hence, a space discretization for the equations (2.12) reads as

$$\begin{aligned} \frac{\varepsilon^2}{\mathcal{V}} \frac{\partial \phi_{i,j}}{\partial t} - \mathcal{D}_h^2 \left(\frac{\varepsilon^2}{3\sigma(\mathbf{x})} \phi \right)_{i,j} + \sigma_a(\mathbf{x}_{i,j}) \phi_{i,j}(t) &= q_{i,j}(t), & t \in (0, T], \\ \frac{2\varepsilon}{3\sigma(\xi_{i,j})} \mathbf{n}(\xi_{i,j}) \cdot \mathcal{D}_h \phi(t, \xi_{i,j}) + \phi(t, \xi_{i,j}) &= g(t, \xi_{i,j}), & t \in (0, T], \\ \phi_{i,j}(0) &= \phi_0(\mathbf{x}_{i,j}), \end{aligned} \quad (5.1)$$

where $\phi_{i,j}(t) = \phi(t, x_i, y_j)$ and the difference notation \mathcal{D}_h^2 is defined by $\mathcal{D}_h^2 = \mathcal{D}_x^2 + \mathcal{D}_y^2$, with

$$\begin{aligned} \mathcal{D}_x^2(\zeta\phi)_{i,j} &= \frac{\zeta_{i,j} + \zeta_{i+1,j}}{2} \frac{\phi_{i+1,j} - \phi_{i,j}}{(\Delta x)^2} - \frac{\zeta_{i-1,j} + \zeta_{i,j}}{2} \frac{\phi_{i,j} - \phi_{i-1,j}}{(\Delta x)^2}, \\ \mathcal{D}_y^2(\zeta\phi)_{i,j} &= \frac{\zeta_{i,j} + \zeta_{i,j+1}}{2} \frac{\phi_{i,j+1} - \phi_{i,j}}{(\Delta y)^2} - \frac{\zeta_{i,j-1} + \zeta_{i,j}}{2} \frac{\phi_{i,j} - \phi_{i,j-1}}{(\Delta y)^2}, \end{aligned}$$

whereas \mathcal{D}_h denotes the difference discretization of the gradient on the boundary approximated by up-winding without using ghost points. All together, the above discretization leads to a system of ordinary differential equations of the form

$$\frac{\varepsilon^2}{\mathcal{V}} \frac{\partial \Phi}{\partial t} = \mathbf{A}\Phi - \mathbf{\Sigma}\Phi + \mathbf{Q}, \quad (5.2)$$

Table 5.1: Error norms obtained for the accuracy test problem using different numbers of gridpoints.

N	L^∞ -error	L^2 -error	CPU (in minutes)
10	3.59E-03	2.01E-03	1.1
20	2.04E-04	1.25E-04	2.9
40	5.68E-06	3.52E-06	8.7
80	1.08E-07	9.47E-08	20.3

where Φ is the solution vector with entries $\phi_{i,j}$, \mathbf{A} is in general a nonsymmetric positive definite matrix obtained from the difference diffusion operator with boundary conditions included, Σ is the diagonal scattering matrix with entries $\sigma_a(\mathbf{x}_{i,j})$, and \mathbf{Q} is a vector containing the right-hand term $q(t)$ and the boundary function g . The system (5.2) can be integrated in time using either an explicit or implicit solver. For example the explicit Euler scheme applied to (5.2) yields

$$\Phi^{n+1} = \Phi^n + \frac{\mathcal{V}\Delta t}{\varepsilon^2} (\mathbf{A}\Phi^n - \Sigma\Phi^n + \mathbf{Q}^n), \quad (5.3)$$

where Δt is the time step and Φ^n denotes the solution at time $t_n = n\Delta t$. Similarly, the implicit Euler scheme can be implemented as

$$\left(\mathbf{I} + \frac{\mathcal{V}\Delta t}{\varepsilon^2}\Sigma - \frac{\mathcal{V}\Delta t}{\varepsilon^2}\mathbf{A}\right)\Phi^{n+1} = \Phi^n + \frac{\mathcal{V}\Delta t}{\varepsilon^2}\mathbf{Q}^{n+1}, \quad (5.4)$$

where \mathbf{I} is the identity matrix. Note that both time-stepping schemes (5.3) and (5.4) are only first-order accurate in time. High-order accuracy can be achieved in time by considering the conventional Runge-Kutta methods, see [10] for a class of linearly implicit Runge-Kutta methods applied to the simplified P_1 problem (2.12) using a finite element method for space discretization. It should also be stressed that because the time-stepping scheme (5.3) evaluates explicitly the right-hand side of the equation (5.2), then it has to satisfy a stability condition. This stability criteria can be derived based on the analysis reported for instance in [24]. Hence, the explicit scheme (5.3) is stable under the condition

$$\frac{\mathcal{V}\Delta t}{3\sigma h^2} \leq \frac{1}{4}, \quad (5.5)$$

where the grid parameter $h = \min(\Delta x, \Delta y)$ and $\sigma = \min_{i,j}(\sigma_{i,j})$. Notice that Δt should depend linearly on the mesh and the total scattering, and reciprocal of the light speed. It can also be observed from the stability restriction (5.5) that, either decreasing the grid spacing h or increasing the speed \mathcal{V} , the explicit scheme (5.3) needs time steps Δt small enough to maintain its stability. On the other hand the implicit scheme (5.4) is unconditionally stable, so that the choice of Δt may be based only on accuracy considerations. However, to find the solution Φ^{n+1} from (5.4) one has to solve, at each time level, a linear system of algebraic equations. In our numerical examples presented in this section we used the GMRES solver with a stopping tolerance of 10^{-6} .

In all the results presented in this section, the radiative speed $\mathcal{V} = 1$ and the optical scale $\varepsilon = 1$. All the computations are made on a Pentium PC with one processor of 518 MB of RAM and 166 MHz. The codes only take the default optimization of the machine, *i.e.* they are not parallel codes.

5.1 Accuracy test problem

In this example we solve the simplified P_1 problem (2.12) in the square domain $\Omega = [0, 1] \times [0, 1]$ using constant scattering and absorption coefficients $\sigma_s = \sigma_a = 1$. The source term q , the boundary function g and the initial datum ϕ_0 are calculated such that the exact solution of (2.12) is given by

$$\phi_e(t, x, y) = \cos(2\pi x) \cos(2\pi y) e^{-t^2}.$$

Table 5.2: Error norms obtained for the accuracy test problem using Hermite polynomials with different orders m .

m	L^∞ -error	L^2 -error	CPU (in minutes)
5	8.57E-01	6.83E-01	0.8
10	5.93E-02	4.73E-02	1.7
20	5.06E-04	3.20E-04	3.3
40	2.04E-04	1.25E-04	6.5

Table 5.3: Relative L^2 -error obtained for the accuracy test problem using frequency-domain method, explicit time-domain and implicit time-domain methods with different time steps Δt .

h	FD method	Explicit TD method			Implicit TD method		
		$\Delta t = 10^{-4}$	$\Delta t = 10^{-3}$	$\Delta t = 10^{-2}$	$\Delta t = 10^{-4}$	$\Delta t = 10^{-3}$	$\Delta t = 10^{-2}$
0.1	4.83E-01	5.25E-01	6.05E-01	7.85E-01	5.06E-01	5.75E-01	6.60E-01
0.05	2.11E-02	7.42E-02	8.48E-02	_____	6.84E-02	7.96E-02	9.32E-02
0.025	1.02E-03	2.28E-02	_____	_____	2.02E-02	2.40E-02	2.86E-02
0.0125	4.13E-04	6.14E-03	_____	_____	5.52E-03	6.71E-03	8.11E-03

The purpose of this test example is to quantify the errors in the proposed frequency-domain method. We consider the relative L^p -norm error function defined as

$$\frac{\|\phi_e - \phi\|_{L^p(\Omega)}}{\|\phi_e\|_{L^p(\Omega)}}, \quad (5.6)$$

where $\|\cdot\|_{L^p(\Omega)}$ is the L^p -norm, ϕ and ϕ_e are respectively, the computed and exact solutions. Only real parts of the obtained solutions are considered. First we check the accuracy of the frequency-domain method with respect to the number of gridpoints used in the computational domain. To this end we set $N_1 = N_2 = N$ and we summarize in Table 5.1 the L^∞ - and L^2 -error norms at time $t = 2.5$ using different values of N and the degree of Hermite polynomials is fixed to $m = 50$. It is evident that increasing the number of gridpoints in the computational domain results in a decrease in all error norms along with an increase in the computational cost. Similar features have been observed for other simulations, not reported here, with different values of the degree of Hermite polynomials m . It should be stressed that the main part of the CPU times listed in Table 5.1 is used by the direct solver for solving the associated linear systems.

Next we examine the accuracy of the frequency-domain method with respect to the order of the Hermite polynomials m . Table 5.2 presents the L^∞ - and L^2 -error norms obtained for $N = 100$ using different values of m . As can be seen from the considered error norms, an increase in the degree of Hermite polynomials yields an increase in the accuracy of the proposed frequency-domain method. Compared to the results in Table 5.1, a slower increase in the CPU times is observed when increasing the degree of Hermite polynomials. As can be observed, there is a little difference between the results obtained using the last polynomial degrees in Table 5.2. For instance, we have found that the discrepancies in the L^2 -error for $m = 10$ and $m = 20$ are less than 0.5%. These differences become less than 0.1% for $m = 20$ and $m = 40$. Therefore, bearing in mind the slight change in the results from $m = 20$ and $m = 40$ at the expense of rather significant increase in CPU times, the simulations with $m = 20$ is believed to be adequate to obtain the results free of interpolation effects. Hence, the results presented herein are based on Hermite polynomials of degrees $m = 20$.

Now we turn our attention to compare the performance of the proposed frequency-domain (FD) method to the well-established time-domain (TD) methods. Here, we consider the explicit TD method

Table 5.4: CPU times (in minutes) obtained for the accuracy test problem using frequency-domain method, explicit time-domain and implicit time-domain methods with different time steps Δt .

h	FD method	Explicit TD method			Implicit TD method		
		$\Delta t = 10^{-4}$	$\Delta t = 10^{-3}$	$\Delta t = 10^{-2}$	$\Delta t = 10^{-4}$	$\Delta t = 10^{-3}$	$\Delta t = 10^{-2}$
0.1	0.2	1.1	0.2	0.03	3.2	1.4	0.8
0.05	0.5	2.3	0.6	_____	6.4	3.0	1.7
0.025	1.2	4.2	_____	_____	13.6	6.6	3.8
0.0125	2.7	8.3	_____	_____	28.4	13.4	9.9

and the implicit TD method given by (5.3) and (5.4), respectively. For the FD method, the degree of Hermite polynomials is fixed to $m = 20$. To quantify the considered methods applied to this example we summarize in Table 5.3 and Table 5.4 the results obtained at time $t = 2.5$ for the relative L^2 -error and the CPU time, respectively. In these tables we present results for different mesh scales $h = \Delta x = \Delta y$ and for different time steps Δt for the TD methods. A simple inspection of these results shows that the implicit TD method can use larger time steps than those required for a stable explicit TD method. It should be noted that using large Δt in the implicit TD method results in a decrease on the number of steps needed to reach the final time $t = 2.5$ and at the same time results in an increase on the number of the iterations in the GMRES solver to reach the tolerance of 10^{-6} . As expected the highest accuracy is obtained for all methods on the fine meshes but with a large CPU time compared to the results on coarse meshes. However, by increasing the time step Δt or decreasing the grid size h the results obtained using the FD method in Table 5.3 and Table 5.4 are more accurate and efficient than results obtained by the TD methods. With increasing Δt for a fixed h , the explicit TD method goes unstable (_____ in Table 5.3 and Table 5.4 corresponds to runs where the explicit TD method becomes unstable) and with decreasing h for a fixed Δt , the computational cost referred to the CPU time in the implicit TD method becomes large. An examination of the relative L^2 -error and the CPU time in the tables also reveals that, both TD methods require finer meshes and more computational work than the FD method for a comparable accuracy.

5.2 Verification test problem

To assess the performance of the proposed frequency-domain method compared to the full radiative transfer, we consider a class of examples by solving the simplified P_1 equations (2.12) in the unit square $\mathcal{D} = [0, 1] \times [0, 1]$ with $q(t, x, y) = 0$ and augmented with the following boundary functions

$$\begin{aligned} g(0, y, \Omega) &= g_{\Gamma_l}(y), & g(1, y, \Omega) &= g_{\Gamma_r}(y), & \text{for } 0 \leq y \leq 1, \\ g(x, 0, \Omega) &= g_{\Gamma_b}(x), & g(x, 1, \Omega) &= g_{\Gamma_t}(x), & \text{for } 0 \leq x \leq 1. \end{aligned}$$

The coefficients σ_s , σ_a , the functions g_{Γ_l} , g_{Γ_r} , g_{Γ_b} and g_{Γ_t} are chosen for four different test problems according to Table 5.5. Initially a vacuum condition is used *i.e.* $\psi_0 = 0$ in (2.3). To solve the full radiative transfer equations (2.1)-(2.3) we use the well-established Diffusion Synthetic Acceleration (DSA) method. The DSA method uses the diffusion approach to accelerate the source iteration which has been widely used in computational radiative transfer. We refer to [25] for the implementation of the method and further discussions on other direct methods can also be found therein. The S_8 discrete-ordinate algorithm (with 80 discrete directions in \mathbb{S}^2) is selected for the discretization of the angle variable and a mesh of 100×100 gridpoints is used in our computations, yielding a linear system with 8×10^5 unknowns which has to be solved for each time step.

In Figure 5.1 we present the distribution of the normalized scalar flux $\phi/4\pi$ obtained by the simplified P_1 and the full radiative transfer for the four test problems from Table 5.5 at the final time $t = 3$. It

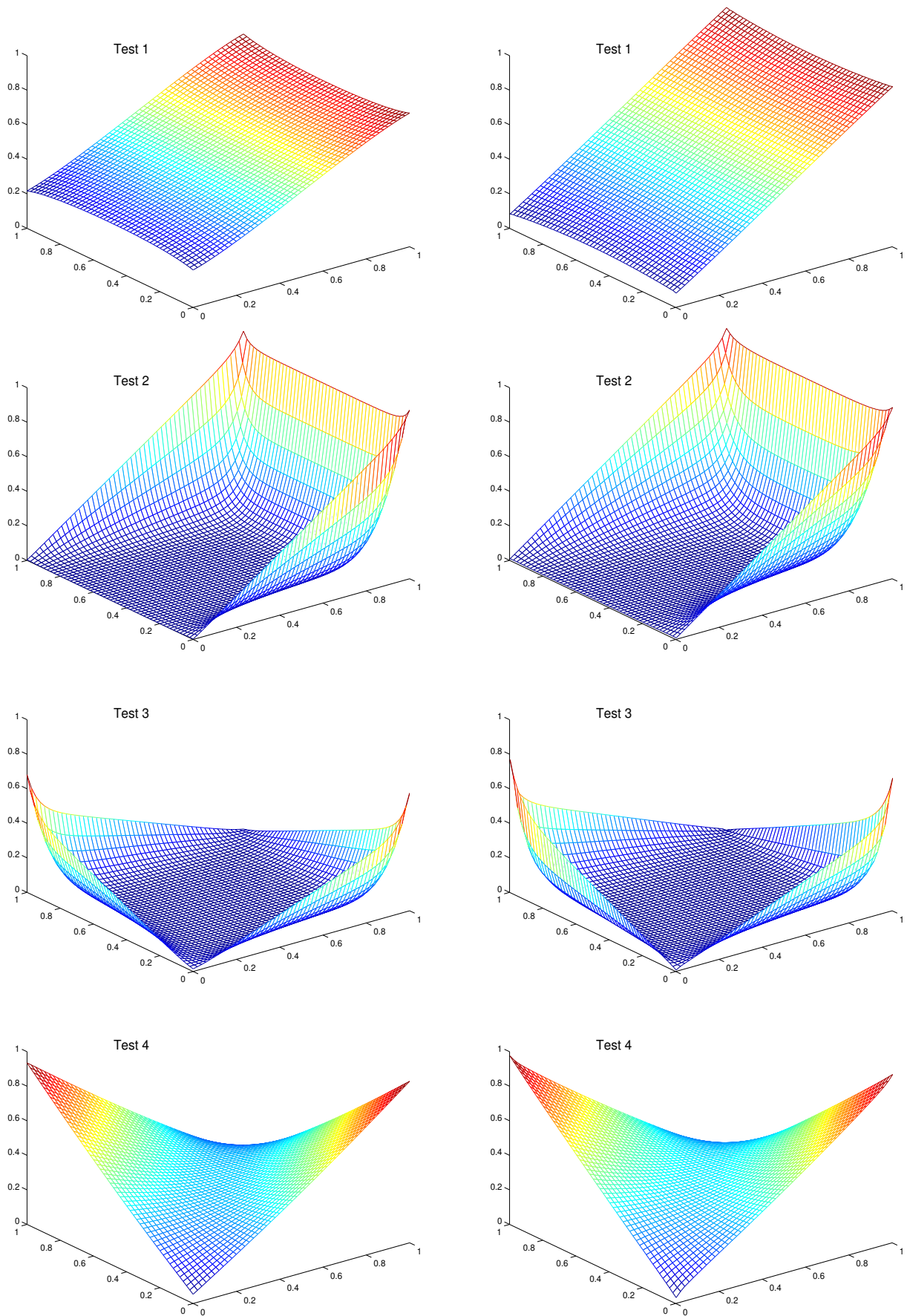


Figure 5.1: Normalized scalar flux at time $t = 3$ obtained using the simplified P_1 (first column) and the radiative transfer solver (second column) for the test examples from Table 5.5.

Table 5.5: Values of σ_s , σ_a and boundary functions for different tests in the verification test problem.

	$\sigma_s(x, y)$	$\sigma_a(x, y)$	$g_{\Gamma_l}(y)$	$g_{\Gamma_r}(y)$	$g_{\Gamma_b}(x)$	$g_{\Gamma_t}(x)$
Test 1	0.99	0.01	0	1	x	x
Test 2	99	1	0	1	x	x
Test 3	1	10	y	$1 - y$	x	$1 - x$
Test 4	10	0	y	$1 - y$	x	$1 - x$

is evident that the proposed frequency-domain method preserves the radiative structures of the scalar fluxes at the optical regimes considered. The boundary features of the scalar fluxes are also captured by our frequency-domain method and they compare well with those obtained using the DSA solver for the full radiative transfer equations (2.1)-(2.3). In order to clearly compare these results, we display in Figure 5.2 a cross section at the main horizontal line $y = 0.5$ of the normalized scalar flux obtained by both methods. It is clear that the results obtained using the simplified P_1 approximation exhibits similar solution trends as the results obtained using the radiative transfer model. As reported in [25], the accuracy of the simplified P_1 approach and the convergence of the DSA method strongly depend on the optical ratio $\epsilon = \frac{1}{\sigma_s + \sigma_a}$ and the scattering ratio $\gamma = \frac{\sigma_s}{\sigma_s + \sigma_a}$. Although, the scattering ratio γ is the same for **Test 1** and **Test 2** ($\gamma = 0.99$), a large discrepancy is detected in the results obtained using the DSA and simplified P_1 methods for **Test 1** which is attributed to the larger value of the optical ratio $\epsilon = 1$ for **Test 1** compared to $\epsilon = 0.01$ for **Test 2**. Similar observations remain valid in **Test 3** and **Test 4** for which ($\gamma = 0.01$, $\epsilon = 0.01$) and ($\gamma = 1$, $\epsilon = 0.1$), respectively. It seems that, for the considered test cases, the simplified P_1 approach asymptotically resolves the radiative transfer equation as the DSA method does, but with very less computational effort referring to the CPU times. It should be noted that when $\gamma \approx 1$ the DSA method converges slowly, for instance, in **Test 2** ($\gamma = 0.99$) DSA needs an average of 280 iterations to converge for a tolerance of 10^{-6} whereas in **Test 4** ($\gamma = 1$) DSA needs only an average of 89 iterations. However, in all tests considered, the frequency-domain method shows fast convergence with a CPU time about 12 times lower than the DSA method. It is also worth remarking that in our simulations the imaginary parts of the solutions are practically zero defined by the machine precision.

5.3 Marshak wave problem

In this test example we solve the two-dimensional version of the Marshak wave studied in [20, 26]. This problem has also been solved in [10] using an adaptive finite element method for spatial discretization and an implicit time integration of Rosenbrock type. The governing equations consist on coupling the simplified P_1 to an energy equation for $\mathbb{B} = a_R \mathcal{T}^4$, with \mathcal{T} is the medium temperature and a_R is the Boltzmann constant,

$$\begin{aligned} \frac{\epsilon^2}{\mathcal{V}} \frac{\partial \phi(t, \mathbf{x})}{\partial t} - \nabla \cdot \left(\frac{\epsilon^2}{3\sigma(\mathbf{x})} \nabla \phi(t, \mathbf{x}) \right) &= \sigma_a(\mathbf{x}) \left(4\pi \mathbb{B}(t, \mathbf{x}) - \phi(t, \mathbf{x}) \right) + q(t, \mathbf{x}), & (t, \mathbf{x}) \in (0, T] \times \Omega, \\ \epsilon^2 \frac{\partial \mathbb{B}(t, \mathbf{x})}{\partial t} &= \sigma_a(\mathbf{x}) \left(\phi(t, \mathbf{x}) - 4\pi \mathbb{B}(t, \mathbf{x}) \right), & (t, \mathbf{x}) \in (0, T] \times \Omega. \end{aligned} \quad (5.7)$$

On the boundary, nonhomogeneous Robin boundary conditions are used

$$\frac{2\epsilon}{3\sigma(\xi)} \mathbf{n}(\xi) \cdot \nabla \phi(\xi, t) + \phi(\xi, t) = 4\pi \mathbb{B}(t, \xi), \quad (t, \xi) \in (0, T] \times \partial\Omega. \quad (5.8)$$

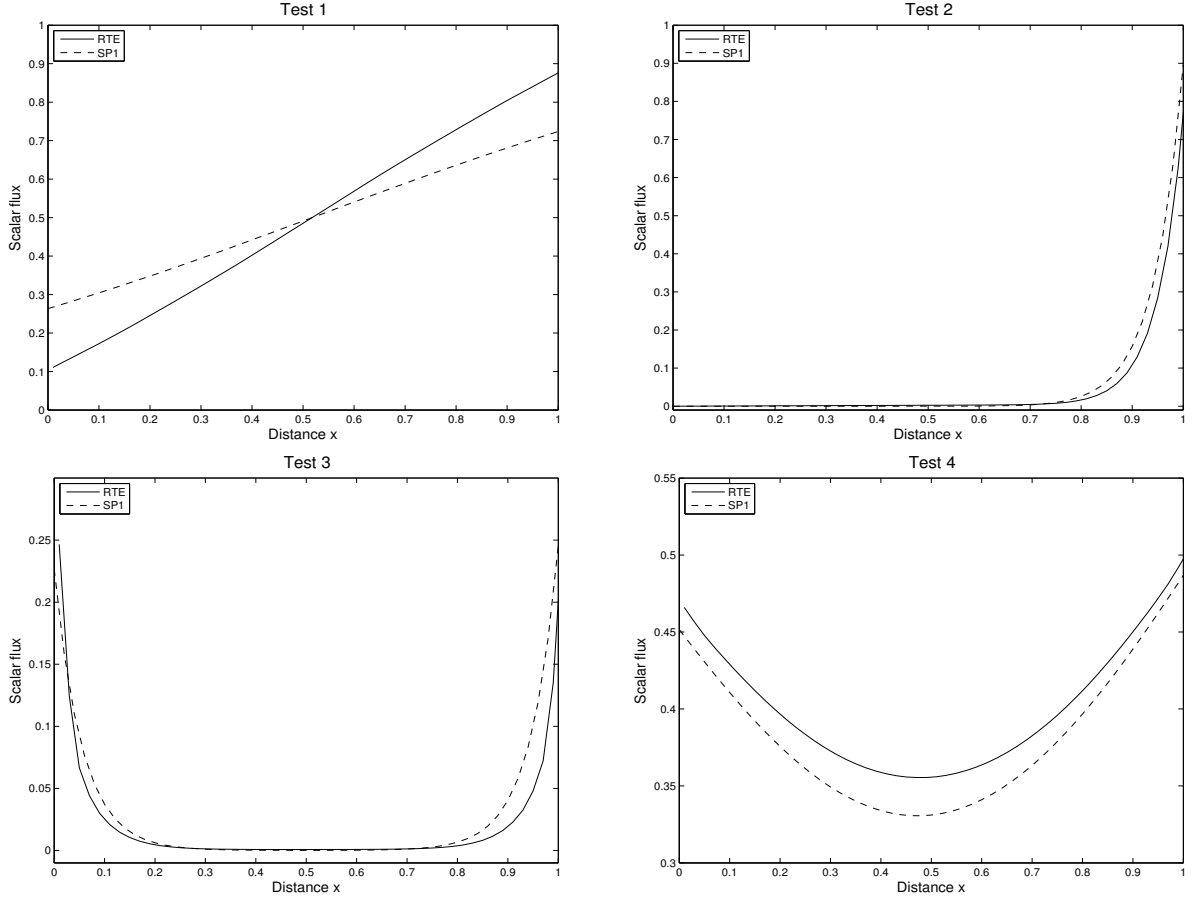


Figure 5.2: Cross sections at $y = 0.5$ of the normalized scalar flux at time $t = 3$ obtained using the simplified P_1 and the radiative transfer solver for the test examples from Table 5.5.

Using the frequency-domain approach described in section 3, the Fourier transform applied to the equations (5.7) and (5.8) yields the following system to be solved for u and v

$$\begin{aligned}
 -\nabla \cdot \left(\frac{\varepsilon^2}{3\sigma(\mathbf{x})} \nabla u(\omega, \mathbf{x}) \right) + \left(\sigma_a(\mathbf{x}) + \frac{i\omega\varepsilon^2}{\mathcal{V}} \right) u(\omega, \mathbf{x}) &= 4\pi\sigma_a(\mathbf{x})v(\omega, \mathbf{x}) + F(\omega, \mathbf{x}), \\
 i\omega\varepsilon^2 v(\omega, \mathbf{x}) + 4\pi\sigma_a(\mathbf{x})v(\omega, \mathbf{x}) &= \sigma_a(\mathbf{x})u(\omega, \mathbf{x}), \quad (\omega, \mathbf{x}) \in \mathbb{R} \times \Omega,
 \end{aligned} \tag{5.9}$$

equipped with the following boundary condition

$$\frac{2\varepsilon}{3\sigma(\xi)} \mathbf{n}(\xi) \cdot \nabla u(\omega, \xi) + u(\omega, \xi) = 4\pi v(\omega, \xi), \quad (\omega, \xi) \in \mathbb{R} \times \partial\Omega, \tag{5.10}$$

where $u(\omega, \cdot) = \widehat{\phi}(\omega, \cdot)$, $v(\omega, \cdot) = \widehat{\mathbb{B}}(\omega, \cdot)$ and $F(\omega, \cdot) = \widehat{q}(\omega, \cdot)$ are the Fourier transforms with respect to the time variable t of $\phi(\cdot, \mathbf{x})$, $\mathbb{B}(\cdot, \mathbf{x})$ and $q(\cdot, \mathbf{x})$, respectively. Similarly, the associated variational problem reads

$$\begin{aligned}
 \int_{\Omega} \frac{\varepsilon^2}{3\sigma(\mathbf{x})} \nabla u(\omega, \mathbf{x}) \overline{\nabla w(\mathbf{x})} d\mathbf{x} + \int_{\Omega} \left(\sigma_a(\mathbf{x}) + \frac{i\omega\varepsilon^2}{\mathcal{V}} \right) u(\omega, \mathbf{x}) \overline{w(\mathbf{x})} d\mathbf{x} + \frac{\varepsilon}{2} \int_{\partial\Omega} u(\omega, \xi) \overline{w(\xi)} d\mu(\xi) \\
 - 4\pi \int_{\Omega} \sigma_a(\mathbf{x}) v(\omega, \mathbf{x}) \overline{w(\mathbf{x})} d\mathbf{x} - 2\pi\varepsilon \int_{\partial\Omega} v(\omega, \xi) \overline{w(\xi)} d\mu(\xi) = \int_{\Omega} F(\omega, \mathbf{x}) \overline{w(\mathbf{x})} d\mathbf{x}, \\
 4\pi \int_{\Omega} \sigma_a(\mathbf{x}) v(\omega, \mathbf{x}) \overline{w(\mathbf{x})} d\mathbf{x} + i\omega\varepsilon^2 \int_{\Omega} v(\omega, \mathbf{x}) \overline{w(\mathbf{x})} d\mathbf{x} - \int_{\Omega} \sigma_a(\mathbf{x}) u(\omega, \mathbf{x}) \overline{w(\mathbf{x})} d\mathbf{x} = 0.
 \end{aligned} \tag{5.11}$$

Note that using the Galerkin projection in $\widehat{\mathbb{V}}_h \times \widehat{\mathbb{V}}_h$, a discrete variational problem can also be formulated in a compact form as (3.16). Hence, the solution pair $(u_h(\omega, \cdot), v_h(\omega, \cdot))$ of the coupled problem (5.9)-(5.10) are given by

$$u_h(\omega, \mathbf{x}) = \sum_{i=1}^{N_1} \sum_{j=1}^{N_2} Z_{h,ij}(\omega) B_{ij}(\mathbf{x}), \quad v_h(\omega, \mathbf{x}) = \sum_{i=1}^{N_1} \sum_{j=1}^{N_2} \tilde{Z}_{h,ij}(\omega) B_{ij}(\mathbf{x}).$$

Substituting these solutions in the variational formulation (5.11) and setting $w(\mathbf{x}) = B_{k\ell}(\mathbf{x})$ we obtain

$$\begin{aligned} \sum_{i=1}^{N_1} \sum_{j=1}^{N_2} Z_{h,ij}(\omega) \left(\frac{\varepsilon^2}{3} D_{ijkl} + U_{ijkl} + \frac{i\omega\varepsilon^2}{\mathcal{V}} C_{ijkl} + Q_{ijkl} \right) - \\ \sum_{i=1}^{N_1} \sum_{j=1}^{N_2} \tilde{Z}_{h,ij}(\omega) \left(4\pi U_{ijkl} + 2\pi\varepsilon Q_{ijkl} \right) = \frac{1}{\varepsilon} \mathbf{B}_{h,k\ell}(\omega) \quad (5.12) \\ \sum_{i=1}^{N_1} \sum_{j=1}^{N_2} \tilde{Z}_{h,ij}(\omega) \left(4\pi U_{ijkl} + i\omega\varepsilon^2 C_{ijkl} \right) - \sum_{i=1}^{N_1} \sum_{j=1}^{N_2} Z_{h,ij}(\omega) U_{ijkl} = 0, \end{aligned}$$

where

$$D_{ijkl} = \int_{\Omega} \frac{1}{\sigma(\mathbf{x})} \nabla B_{ij}(\mathbf{x}) \nabla B_{k\ell}(\mathbf{x}) d\mathbf{x}, \quad U_{ijkl} = \int_{\Omega} \sigma_a(\mathbf{x}) B_{ij}(\mathbf{x}) B_{k\ell}(\mathbf{x}) d\mathbf{x}, \quad C_{ijkl} = \int_{\Omega} B_{ij}(\mathbf{x}) B_{k\ell}(\mathbf{x}) d\mathbf{x},$$

and

$$Q_{ijkl} = \int_{\partial\Omega} B_{ij}(\xi) B_{k\ell}(\xi) d\mu(\xi), \quad \mathbf{B}_{h,k\ell}(\omega) = \frac{1}{\varepsilon} \int_{\Omega} F(\omega, \mathbf{x}) B_{k\ell}(\mathbf{x}) d\mathbf{x},$$

for $i, k = 1, \dots, N_1$ and $j, \ell = 1, \dots, N_2$. The discrete variational form (5.12) leads to the linear system

$$\begin{pmatrix} \frac{i\omega\varepsilon^2}{\mathcal{V}} C + \frac{\varepsilon^2}{3} D + U + \frac{\varepsilon}{2} Q & -4\pi U - 2\pi\varepsilon Q \\ -U & i\omega\varepsilon^2 C + 4\pi U \end{pmatrix} \begin{pmatrix} z_h(\omega) \\ \tilde{z}_h(\omega) \end{pmatrix} = \begin{pmatrix} \frac{1}{\varepsilon} \mathbf{b}_h(\omega) \\ 0 \end{pmatrix}, \quad (5.13)$$

where $\mathbf{b}_h(\omega)$, $z_h(\omega)$ and $\tilde{z}_h(\omega)$ are $N_1 N_2$ vectors the entries of which are the complex coefficient $\mathbf{B}_h(\omega)$, $Z_h(\omega)$ and $\tilde{Z}_h(\omega)$, respectively.

For the Marshak wave problem proposed in [20, 26], we solve the system (5.7) in an initially empty medium $\mathcal{D} = [0, 5x_0] \times [0, 5x_0]$ subject to an instantaneous spatially bounded source q defined by

$$q(t, \mathbf{x}) = \begin{cases} \frac{1}{4x_0^2}, & \text{for } 0 \leq t \leq T, \quad \mathbf{x} \in \Omega_0, \\ 0 & \text{otherwise,} \end{cases}$$

where $\Omega_0 = [-x_0, x_0] \times [-x_0, x_0]$. For the simulation reported in this section, $x_0 = 0.5$, $\sigma_s = 0$, $\sigma_a = 1$ and $T = 10$. We consider two meshes with 50×50 and 100×100 gridpoints and the mean radiative flux ϕ is displayed at two different instants $t = 1$ and $t = 10$. Figure 5.3 presents the surface plots of the mean radiative intensity whereas, cross sections of these results at the boundary edge $y = 0$ are depicted in Figure 5.4. Due to the source located at the domain origin a radiative wave develops and propagates along the main diagonal in the computational domain. The wave amplitude increases within the time until the source is switched off at time $t = 10$ and after this time the radiative wave dissipates towards the far end

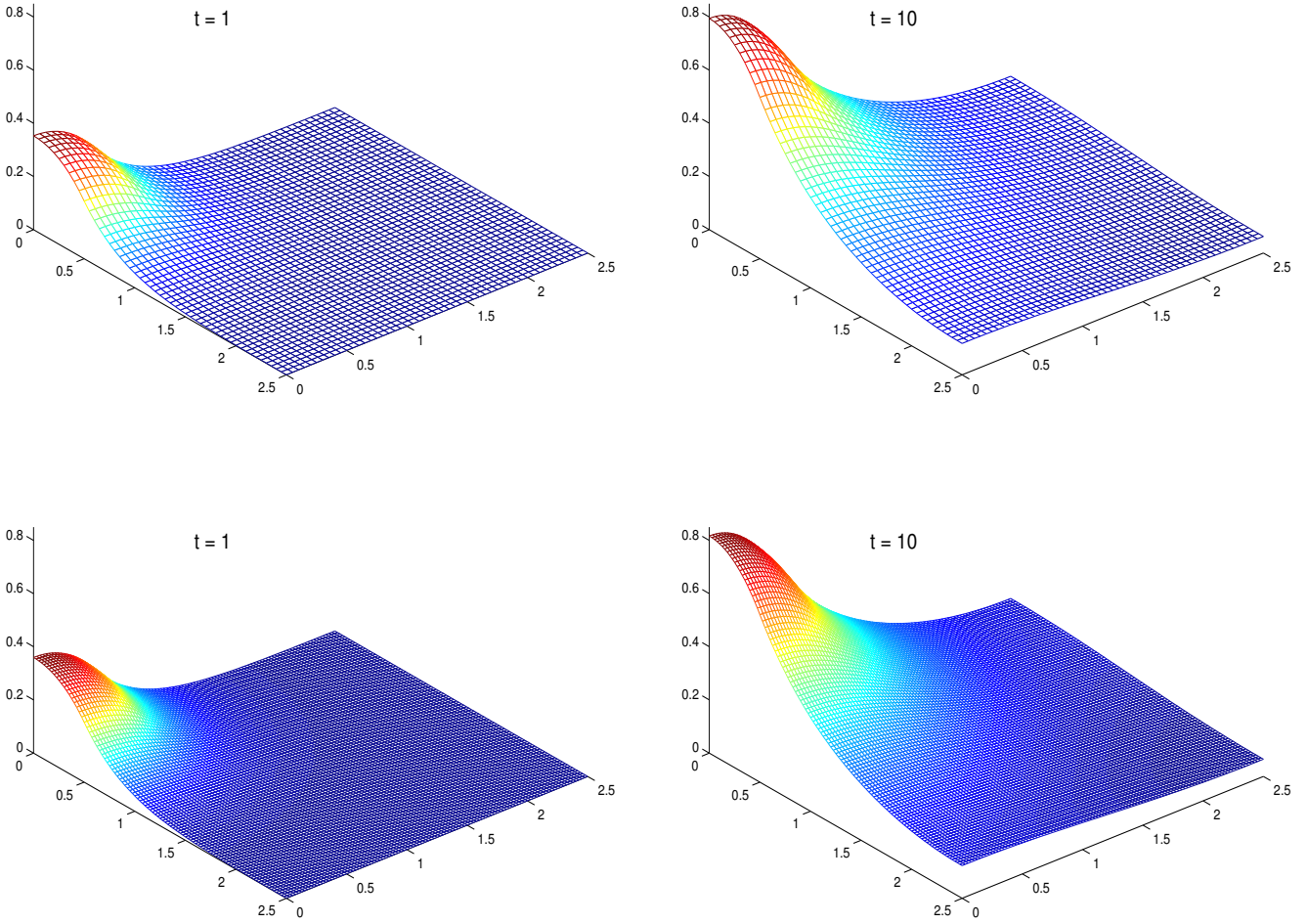


Figure 5.3: The scalar flux obtained for the Marshak problem on a mesh with 50×50 gridpoints (top) and a mesh with 100×100 gridpoints (bottom) at two different instants $t = 1$ (left) and $t = 10$ (right).

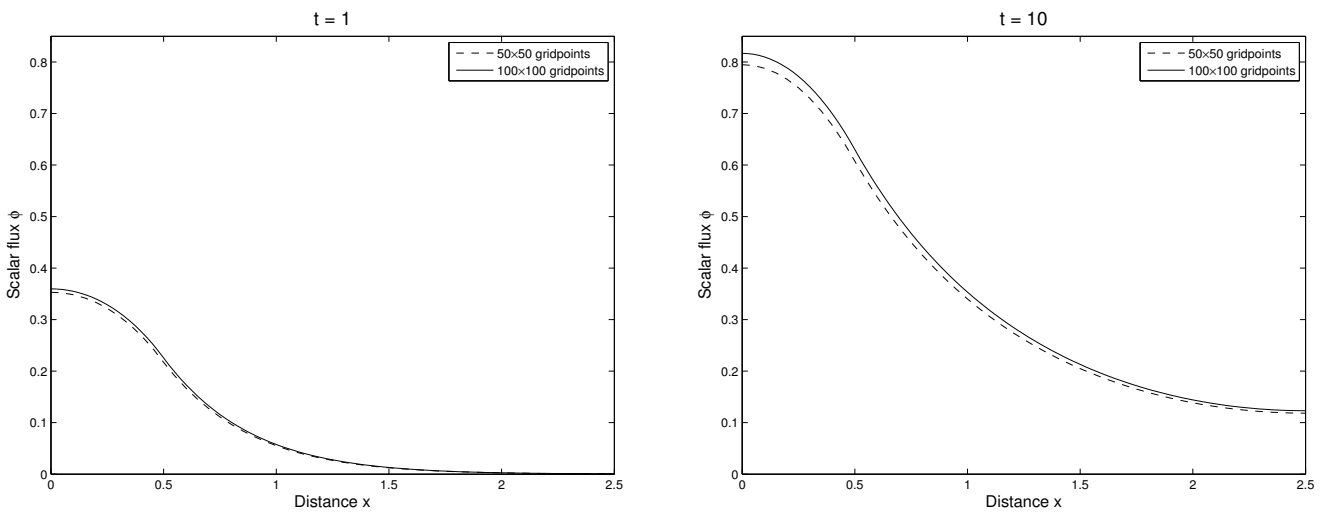


Figure 5.4: Cross sections at $y = 0$ of the scalar flux at time $t = 1$ (left) and $t = 10$ (right) obtained for the Marshak problem on two different meshes with 50×50 and 100×100 gridpoints.

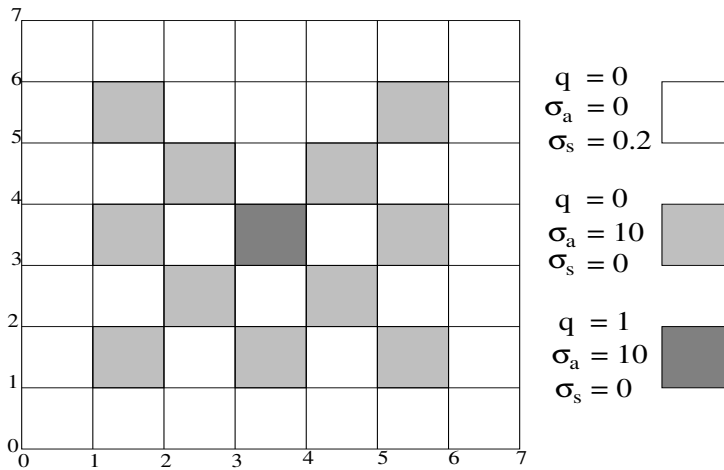


Figure 5.5: Configuration for the test example of lattice problem.

boundary of the domain. These results agree very well with those reported in [10] obtained using a time-domain approach in the finite element framework. In [10] the authors have employed h -adaptive finite element methods resulting in an excessive fine mesh to accurately resolve the radiative shock. Remark that the results obtained on the coarse mesh with 50×50 gridpoints exhibits small numerical diffusion compared to those obtained on the fine mesh with 100×100 gridpoints, compare the cross-section plots in Figure 5.4. Again the obtained results demonstrate the ability of the presented frequency-domain method to capture the radiative wave propagation without generating non-physical oscillations. The proposed frequency-domain method performs very satisfactorily for this nonlinear coupled problem since it does not diffuse the moving fronts and no spurious oscillations have been detected near steep gradients of the temperature field and the radiative flux in the computational domain.

5.4 Lattice problem

Our final test example is the lattice problem of radiation propagation in a two-dimensional checkerboard structure of materials with different optical properties [6]. This problem has also been studied in [9, 10] using time-domain discretizations and we consider the same set-up and the same parameters in our simulations. Thus, the configuration of this problem is shown in Figure 5.5 where a source is switched on at $t = 0$ and the final time is $t = 2$. It is expected, due to different scattering and absorbing areas in the computational domain, that the radiation field leaks through the squares. The purpose of this test problem is to demonstrate the ability of the frequency-domain method to compute accurate solutions for simplified P_1 approximation of radiative transfer problems in heterogeneous media with discontinuous scattering and absorption coefficients. Note that for this test example the considered radiative transfer equation is solved with a zero scattering and absorption coefficients in some parts of the computational domain. As a consequence, this radiative transfer problem is more difficult to handle; the results shown here illustrate the robustness of the frequency-domain method. Furthermore, the considered radiative transfer example is a problem unsteady in nature; therefore, good numerical accuracy is required in order to capture the different phenomena present in its evolving solution. The frequency-domain method shows high accuracy and good stability for this transient radiative transfer problem.

In Figure 5.6 we present the snapshots of the scalar radiative flux at time $t = 2$ using two meshes with 100×100 and 200×200 gridpoints. As suggested in [9, 10] we display the results as decimal logarithm of the scalar radiative flux (*i.e.* $\log_{10} \phi$). The presented radiative patterns are in good agreement with those reported in [9, 10] for the transient simplified P_1 approximation of this radiative heat transfer example. To clearly visualizing the effects of grids on the frequency-domain solution of this example, we illustrate the cross sections of the scalar flux at the central line $y = 3.5$. Under the actual radiative conditions, it

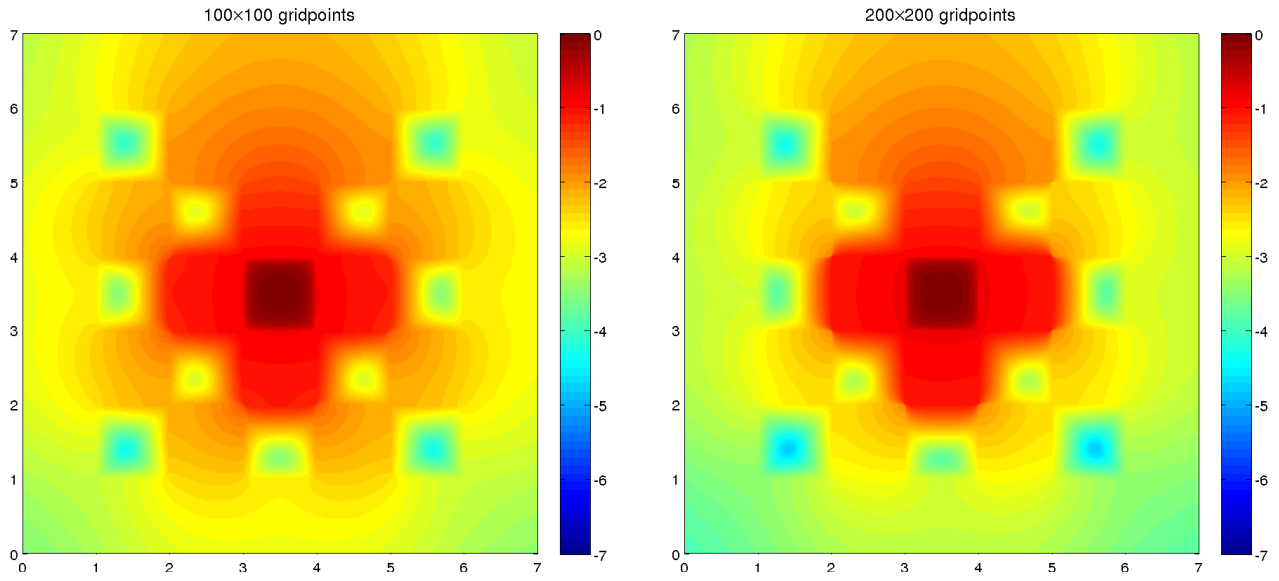


Figure 5.6: The scalar flux $\log_{10}(\phi)$ obtained for the lattice problem at time $t = 2$ using a mesh with 100×100 gridpoints (left) and a mesh with 200×200 gridpoints (right).

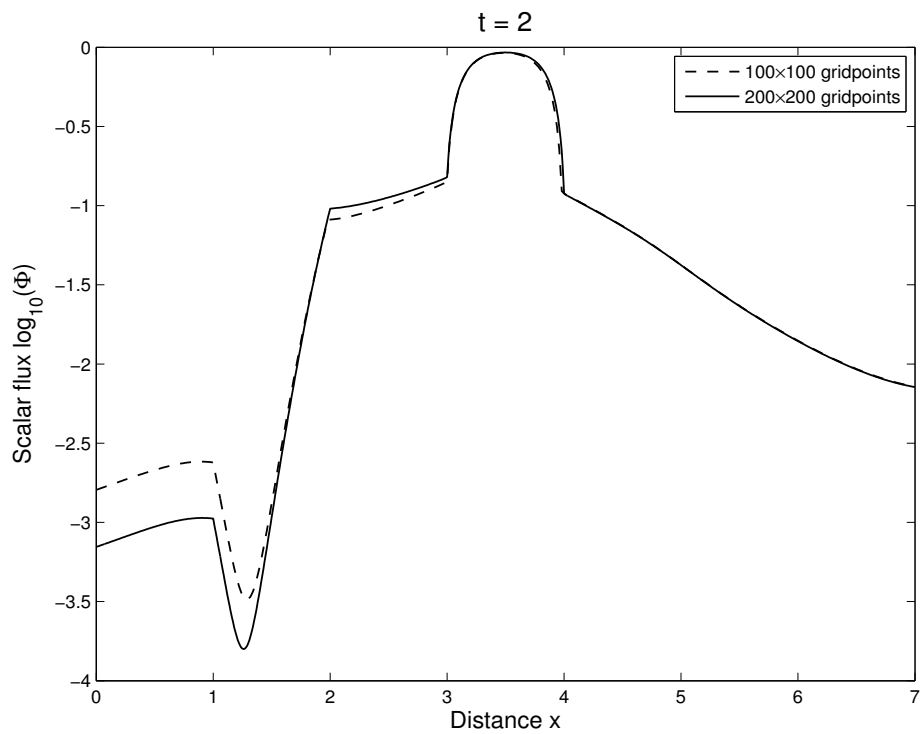


Figure 5.7: Cross sections at $y = 3.5$ of the scalar flux $\log_{10}(\phi)$ at time $t = 2$ obtained for the lattice problem using two different meshes.

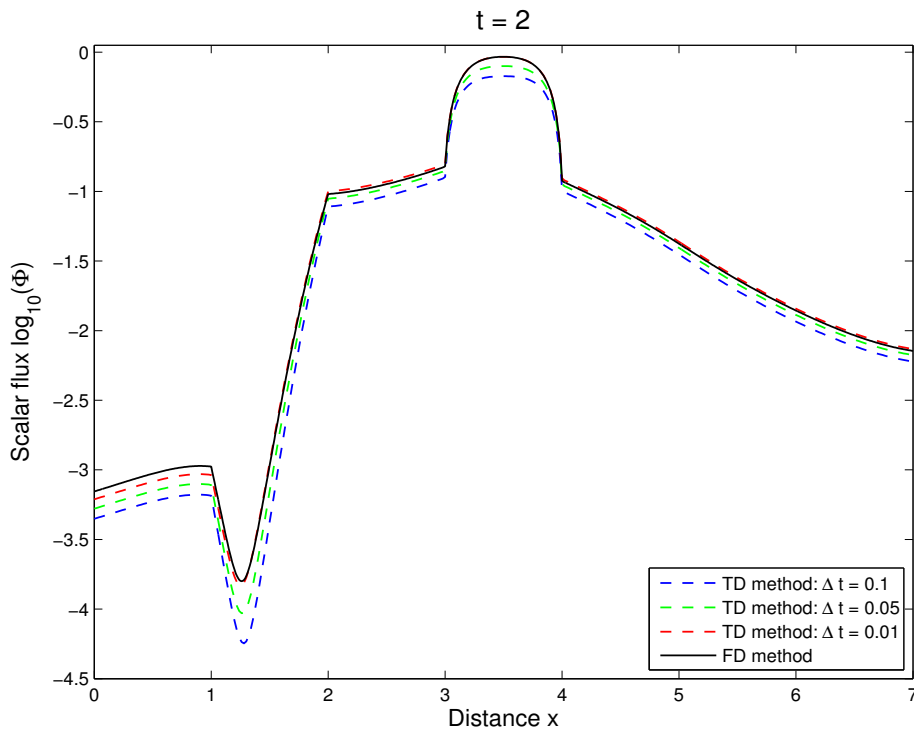


Figure 5.8: Comparison results for cross sections at $y = 3.5$ of the scalar flux $\log_{10}(\phi)$ at time $t = 2$ obtained for the lattice problem using the frequency-domain and time-domain methods.

is clear that the scalar radiative flux on the coarse mesh exhibited a different behavior in the left area to the source and results obtained on the fine mesh are the most accurate. Similar features have been observed for a comparison, not reported here, of cross sections at $y = 3.5$. The computed results also verify the stability and the non-oscillatory properties of the considered frequency-domain method. Note that the performance of the proposed frequency-domain method is very attractive since the computed solutions remain stable and oscillation-free even on coarse meshes without solving nonlinear systems or requiring fronts tracking techniques.

Finally we compare the results obtained for this test problem using the proposed frequency-domain method to those obtained using the time-domain methods. To this end we solve this problem using the implicit time-domain method (5.4) using different time steps. The explicit time-domain method is not considered in these simulations because of the severe restriction on the time step Δt required to ensure its stability. We have also found for a comparable set of results for the considered methods, extensive fine meshes are needed for the time-domain method than its frequency-domain counterpart. Here a mesh of 400×400 gridpoints is used for the implicit TD method and different values of Δt are considered to assess its performance. In the FD method a mesh of 200×200 gridpoints is used and the order of Hermite polynomials is set to $m = 20$. The obtained cross sections at $y = 3.5$ of the scalar flux $\log_{10}(\phi)$ at time $t = 2$ are depicted in Figure 5.8. As can be seen from these results the numerical diffusion is more pronounced in the TD methods with large time steps than the FD method. This numerical diffusion is reduced by decreasing the values of time step which results in an increase of the total steps needed to reach the time $t = 2$. Under the considered radiative conditions, the proposed frequency-domain method is more accurate and efficient than the implicit time-domain method. It should be noted that the frequency-domain method uses only half of gridpoints than the time-domain method and its about five times faster than the time-domain method with $\Delta t = 0.01$.

6 Conclusions

In this article we have presented a new frequency-domain method to solve the simplified P_1 approximation of time-dependent radiative transfer equations. The method consists of two stages which can be interpreted as a forward-backward procedure. In the forward stage, the simplified P_1 equations are transformed into an elliptic problem for the frequency variables using the Fourier transform. Using this technique we avoid the time restriction that may occur in the time-domain solution of the equations. As a solver for the forward problem we have developed a Galerkin projection method based on the tensor-product B-spline interpolants. In the backward stage, solution of the inverse Fourier transform is obtained using a Gauss-Hermite quadrature method. The considered method is simple, stable and eliminates the numerical difficulties related to the discretization of the time variable in the time-dependent simplified P_1 equations. Verification of the proposed method has been carried out using several test problems in transient radiative transfer modeling for smooth and discontinuous solutions. The method exhibited good shape, high accuracy and stability behavior for all radiative regimes considered. The presented results demonstrate the capability of the frequency-domain method that can provide insight to complex radiative transfer behaviors.

Future work will concentrate on developing efficient iterative solvers for the linear systems resulting in both the forward and backward problems and also on performing computations for time-dependent simplified P_1 problems in three space dimensions. Furthermore, it is worth emphasizing that, the simplified P_1 model considered in the current work is only valid at the diffusive regime of the radiative transfer. However, the results make it promising to be applicable also to higher order simplified P_N approximations in real situations where, beyond the many sources of complexity, there is a more severe demand for accuracy in predicting the radiative energy, which must be performed for long simulation times.

Acknowledgment. This work was partly performed while the third author was visiting LMPA at Université Lille-Nord de France. Financial support provided by LMPA is gratefully acknowledged.

References

- [1] M. Abramowitz and I.A. Setgun (Eds). *Handbook of mathematical functions with formulas, graphs, and mathematical tables, 9th printing*. New York: Dover, 1972.
- [2] M. Addam. *Approximation du problème de diffusion en tomographie optique et problème inverse*. PhD thesis, LMPA, Université Lille-Nord de France, 2010.
- [3] M. Addam, A. Bouhamidi, and K. Jbilou. Signal reconstruction for the diffusion transport equation using tensorial spline galerkin approximation. *Applied Numerical Mathematics*, 62:1089–1108, 2012.
- [4] A.M. Anile, S. Pennisi, and M.A. Sammartino. A thermodynamical approach to Eddington factors. *J. Math. Phys.*, 32:544–550, 1991.
- [5] R. Backofen, T. Bilz, A. Ribalta, and A. Voigt. SP_N -approximations of internal radiation in crystal growth of optical materials. *J. Crystal Growth.*, 266:264–270, 2004.
- [6] T.A. Brunner and J.P. Holloway. Two-dimensional time dependent riemann solvers for neutron transport. *J. Comput. Phys.*, 210:386–399, 2005.
- [7] G.A. Campbell and R.M. Foster. *Fourier Integrals for Practical Applications*. D. Van Nostrand Company, Inc., New York, 1948.
- [8] W. Fiveland. The selection of discrete ordinate quadrature sets for anisotropic scattering. *ASME HTD. Fundam. Radiat. Heat Transfer.*, 160:89–96, 1991.

- [9] M. Frank, A. Klar, E.W. Larsen, and S. Yasuda. Time-dependent simplified P_N approximation to the equations of radiative transfer. *J. Comput. Phys.*, 226:2289–2305, 2007.
- [10] M. Frank, L. Lang, and M. Schäfer. Adaptive finite element simulation of the time-dependent simplified P_N equations. *Journal of Scientific Computing*, 226:2289–2305, 2007.
- [11] E.M. Gelbard. *Simplified Spherical Harmonics Equations and their Use in Shielding Problems*. Technical Report WAPD-T-1182, Bettis Atomic Power Laboratory, 1961.
- [12] D. Gorpas, D. Yova, and K. Politopoulos. A three-dimensional finite elements approach for the coupled radiative transfer equation and diffusion approximation modeling in fluorescence imaging. *Journal of Quantitative Spectroscopy and Radiative Transfer*, 111:553–568, 2010.
- [13] A.D. Klose and E.W. Larsen. Light transport in biological tissue based on the simplified spherical harmonics equations. *J. Comput. Phys.*, 220:441–470, 2006.
- [14] A.D. Klose and T. Poschinger. Excitation-resolved fluorescence tomography with simplified spherical harmonics equations. *Phys. Med. Biol.*, 56:1443–1469, 2011.
- [15] P. Kotiluoto. *Adaptive tree multigrids and simplified spherical harmonics approximation in deterministic neutral and charged particle transport*. PhD thesis, University of Helsinki, VTT Technical Research Centre of Finland, 2007.
- [16] E. Larsen, J. Morel, and J. McGhee. Asymptotic derivation of the multigroup P_1 and simplified P_N equations with anisotropic scattering. *Nucl. Sci. Eng.*, 123:328–367, 1996.
- [17] E. Larsen, G. Thömmes, A. Klar, M. Seaid, and T. Götz. Simplified P_N approximations to the equations of radiative heat transfer and applications. *J. Comp. Phys.*, 183:652–675, 2002.
- [18] E.W. Larsen. Diffusion theory as an asymptotic limit of transport theory for nearly critical systems with small mean free paths. *Ann. Nucl. Energy.*, 7:249–255, 1980.
- [19] E. Lewis and W. Miller. *Computational Methods of Neutron Transport*. John Wiley & Sons, New York, 1984.
- [20] R.E. Marshak. Note on the spherical harmonic method as applied to the milne problem for a sphere. *Phys. Rev.*, 71:443–446, 1947.
- [21] D. Mihalas and B.S. Mihalas. *Foundations of Radiation Hydrodynamics*. Oxford University Press, New York, 1983.
- [22] M.F. Modest. *Radiative Heat Transfer*. McGraw-Hill, 1993.
- [23] G.C. Pomraning. *The Equations of Radiation Hydrodynamics*. Pregamon press, 1973.
- [24] J.M. Sanz-Serna and A.M. Stuart. A note on uniform in time error estimates for approximations to reaction-diffusion equations. *IMA J. Numer. Anal.*, 12:457–462, 1992.
- [25] M. Seaid and A. Klar. Efficient preconditioning of linear systems arising from the discretization of radiative transfer equation. *Lect. Notes. Comp. Sci.*, 35:211–236, 2003.
- [26] B. Su and G.L. Olson. An analytical benchmark for non-equilibrium radiative transfer in an isotropically scattering medium. *Ann. Nucl. Energy*, 24:1035–1055, 1997.
- [27] T. Tarvainen, V. Kolehmainen, S.R. Arridge, and J.P. Kaipio. Image reconstruction in diffuse optical tomography using the coupled radiative transport-diffusion model. *Journal of Quantitative Spectroscopy and Radiative Transfer*, 112:2600–2668, 2011.

- [28] I. Teleaga and M. Seaid. Simplified radiative models for low mach number reactive flows. *Applied Mathematical Modelling.*, 32:971–991, 2009.
- [29] G. Thömmes, R. Pinnau, M. Seaid, T. Götz, and A. Klar. Numerical methods and optimal control for glass cooling processes. *Transp. Theory Stat. Phys.*, 31:513–529, 2002.
- [30] R. Viskanta and E.E. Anderson. Heat transfer in semitransparent solids. *Advances in Heat Transfer*, 11:317–441, 1975.